RSC Advances

PAPER

View Article Online
View Journal | View Issue

Cite this: *RSC Adv.*, 2024, **14**, 28182

Carbon and boron nitride quantum dots as optical sensor probes for selective detection of toxic metals in drinking water: a quantum chemical prediction through structure- and morphology-dependent electronic and optical properties†

Chedharla Balaji Sarath Kumar, [a] Rence Painappallil Reji, [a] Yuvaraj Sivalingam, [bc] Yoshiyuki Kawazoe[de] and Velappa Jayaraman Surya *[ad]

Toxic metals present in drinking water pose a serious threat to the environment and human beings when present in abundance. In this work, we investigated the sensing ability of quantum dots (pristine CQDs, boron/nitrogen/sulphur (B/N/S)-doped CQDs, and BNQDs) of various sizes and morphologies (rectangular, circular, and triangular) towards toxic metals such as arsenic (As), cobalt (Co), nickel (Ni), copper (Cu), and lead (Pb) using quantum chemical density functional theory calculations in both gas and water phases. We probed the structural, electronic, and optical properties of the QDs. All the modelled QDs are energetically stable. Frontier molecular orbital analysis predicted that BNQDs are more chemically stable than all other CQDs. UV-vis absorption and Raman spectra analyses helped to understand the optical properties of all the QDs. Further, adsorption studies revealed that triangular pristine CQDs and sulphur-doped CQDs show higher adsorption affinity towards the toxic metals. The magnitude of adsorption energies follows the trend Ni > Pb > As > Cu > Co in most of the QDs. Several pristine and doped CQDs exhibited chemisorption towards the toxic metals, and hence, they can be used as adsorbents. However, a majority of BNQDs showed physisorption towards the metals, and therefore, they can be used as efficient optical sensors compared to CQDs. Further, the sensing ability of the QDs was explored through optical phenomena such as changes in UV-vis absorption spectra and fluorescence after metal adsorption. When compared to pristine CQDs and B/N/S-doped CQDs, metal complexation caused significant changes in the UV-vis absorbance peak intensities in BNQDs along with peak shifts. Moreover, metal interaction with the QDs increased their fluorescence lifetime with the highest values observed in Co-adsorbed triangular $H_{18}C_{46}$ (152.30 ns), Pb-adsorbed rectangular $H_{15}C_{30}S$ (21.29 ns), and As-adsorbed circular $B_{27}N_{27}H_{18}$ (2.99 μs) among pristine CQDs, B/N/S-doped CQDs, and BNQDs, respectively. Overall, we believe that our first-of-its-kind computational prediction of the optical sensing ability of tailor-made zero-dimensional systems such as QDs will be a great aid for experimentalists in designing novel and rapid optical probes to detect toxic metals in drinking water.

Received 4th July 2024
Accepted 12th August 2024

DOI: 10.1039/d4ra04843a

rsc.li/rsc-advances

1. Introduction

The very existence of life on Earth depends on water, critically. The composition of cells and the transport of nutrients into the cells as well as the metabolism of the body depend on water. Currently, water pollution is one of the serious issues faced by all living forms, including humans and aquatic animals. The availability of limited freshwater resources worldwide has resulted in severe water scarcity, affecting 4 billion people for at least one month annually. Approximately 2.2 billion people lack

[a]*Novel, Advanced, and Applied Materials (NAAM) Laboratory, Department of Physics and Nanotechnology, SRM Institute of Science and Technology, Kattankulathur 603203, Tamil Nadu, India. E-mail: suryaj@srmist.edu.in*

[b]*Laboratory of Sensors, Energy and Electronic Devices (Lab SEED), Department of Physics and Nanotechnology, SRM Institute of Science and Technology, Kattankulathur 603203, Tamil Nadu, India*

[c]*Computer, Electrical and Mathematical Sciences and Engineering Division (CEMSE), King Abdullah University of Science and Technology (KAUST), Thuwal 23955-6900, Kingdom of Saudi Arabia*

[d]*New Industry Creation Hatchery Center, Tohoku University, Aoba-ku, Miyagi, Sendai 980-8579, Japan*

[e]*Department of Physics and Nanotechnology, SRM Institute of Science and Technology, Kattankulathur 603203, Tamil Nadu, India*

† Electronic supplementary information (ESI) available: ESP plots of all QDs, HOMO–LUMO plots of rectangular QDs, Raman spectra of all QDs, Optimized structures of QDs + metal complexes, Formation energies of Metal–QD complexes in gas and water phases, dipole moments of all QDs before and after metal interaction. See DOI: https://doi.org/10.1039/d4ra04843a

access to clean drinking water globally.[1] According to reports from the World Health Organization (WHO), due to contamination of drinking water, diseases such as diarrhoea kill 485 000 people annually.[2] The demand for clean drinking water has increased. However, due to population explosion, urbanization, advancement in technology, and growth of industries, freshwater sources that provide drinking water are under threat. Many toxic elements are released into water without proper drainage/chemical treatment. Major sources that are responsible for the contamination of drinking water are fertilizers, tanning, soldering, electroplating, pesticides, batteries, and pipe manufacturing industries and they accumulate toxic metals in excess concentration.[3] Due to this issue, our ecosystem and human health are under serious threat. The accumulation of metals such as copper (Cu), lead (Pb), arsenic (As), cobalt (Co), and nickel (Ni) in drinking water has raised a great concern worldwide as the excess concentration of these metals in water can lead to adverse health effects. Arsenic (As) contamination of water arises from smelting, pesticides, fungicides, and glass production industries.[4–6] The most common oxidation states of As ions in water are +3 and +5.[7] Long-term exposure to As through water beyond the permissible limit leads to bronchitis, dermatitis, hypopigmentation, hyperkeratosis, and encephalopathy.[4,5] The maximum permissible limit of As ions in drinking water set by the WHO is 0.01 mg L^{-1}.[5,8] Lead (Pb) is one of the heavy metals arising from automobile emissions, mining sources, lead-based batteries, leaded fuels, and pesticides. The oxidation state of lead ions in water varies from +2 to +4 but the most common oxidation state of lead is +2.[9] Prolonged exposure of humans to lead in excess concentrations through water causes damage and malfunctioning of the liver, kidney and reproductive system.[8] The maximum contaminant level of Pb ions in drinking water set by the WHO is 0.1 mg L^{-1}.[5,6] Copper (Cu) is one of the essential elements for humans and is necessary in trace amounts in our diet to ensure good health. Excessive accumulation of copper in water arises from ore refineries, pesticides, fertilizers, and smelting.[5] The Cu ion in water has an oxidation state of +1 and +2.[7] Continued exposure to Cu through water leads to gastrointestinal irritation, hemolysis, anaemia, and multiorgan dysfunction syndrome.[5,6] The maximum permissible limit of Cu ions in drinking water set by the WHO is 0.1 mg L^{-1}.[5,6] Nickel (Ni) is one of the transition metals arising from steel, alloy production, automobile batteries, and surgical instrument industries.[4,5] The most common oxidation state of Ni ions in water is +2.[7] Prolonged exposure to Ni through water leads to pulmonary fibrosis, dermatitis, gastrointestinal distress, myocarditis, and encephalopathy[4,5] The maximum permissible limit of Ni ions in drinking water set by the WHO is 0.2 mg L^{-1}.[5] Cobalt (Co) contamination of water arises from hard metal production, diamond, paint, and electronic waste recycling industries.[10] The most common oxidation states of Co ions in water are +2 and +3.[7] Long-term exposure to Co through water beyond the permissible limit causes damage to the cardiovascular and pulmonary systems.[7] The maximum permissible limit of Co ions in drinking water set by the United States Environmental Protection Agency is 100 μg L^{-1}.[11]

Recently, there has been a steady increase in interest in employing quantum dots (QDs) for the detection and removal of toxic metals in drinking water. In this quantum materials era, carbon quantum dots (CQDs) that are zero-dimensional fluorescent nanomaterials with a size range of less than 20 nm have attracted considerable attention in recent years because of their immense potential and use in a wide range of applications such as biosensing,[12] bioimaging,[13] photodynamic therapy,[14] and electrocatalysis.[15] CQDs were chosen for the detection of metals because of their distinct properties such as harmless chemical composition (environment friendly), modifiable fluorescence, simple functionalization, tunable optical properties, good fluorescence properties, large surface area, and good physicochemical and photochemical stability.[16–22] Heteroatom doping of CQDs with non-metallic elements such as boron (B), nitrogen (N), and sulphur (S) is one of the efficient approaches to alter the chemical composition and to improve the electronic and optical properties of CQDs.[19,23,24] Similar to CQDs, BNQDs are metal-free quantum dots, which are made up of non-toxic elements such as B, and N. They are chosen as optical probes for the detection of metals because they are environment-friendly, possess a large surface area, and have polar B–N bonds.[25–27] Moreover, they have been continuously explored for various applications such as optoelectronics,[28] biomedicine,[29] photocatalysis,[30] and organic pollutant adsorption due to their unique properties such as good electrical insulation, optical properties, chemical stability, thermal stability, high mechanical strength, and low toxicity.[31] The detection of metals using various types of QDs has been investigated in detail by earlier reports using the optical sensing method.[32–34] Recently, there have been many reports on the detection of toxic metals such as Pb and Ni in water using carbon nanomaterials.[18,35] Moreover, BNQDs have been used for the detection of toxic metals in water. Yao *et al.*, reported the detection of Ni^{2+} ions in water using BNQDs *via* a quenching mechanism.[36] Liu *et al.* investigated the detection of Pb^{2+} and Cu^{2+} ions in water using BNQDs *via* a quenching mechanism.[37]

In this work, we investigated the potential of various QDs such as pristine CQD, B/N/S-doped CQDs, and BNQDs of different sizes and morphologies (rectangular, circular, and triangular) to detect toxic elements As, Co, Ni, Cu, and Pb using quantum chemical density functional theory (DFT) calculations. We carried out the structural assessment of the QDs *via* formation energy analysis. The electronic properties were understood through the highest occupied molecular orbital (HOMO), lowest unoccupied molecular orbital (LUMO), and energy gap analyses. Moreover, optical properties were explored by UV-vis and Raman spectra analyses. The adsorption behaviour of the QDs towards As, Cu, Co, Ni, and Pb in both gas and water phases was investigated. To substantiate the optical sensing ability of the designed QDs, the changes in UV-vis absorption spectra and fluorescence properties were investigated before and after the interaction of toxic elements with them in the water phase. To the best of our knowledge, this is the first report on computational assessment of the detection of toxic elements using QDs of various sizes and morphologies based on the optical transduction mechanism using UV-vis absorption spectra in the water phase. We believe that our

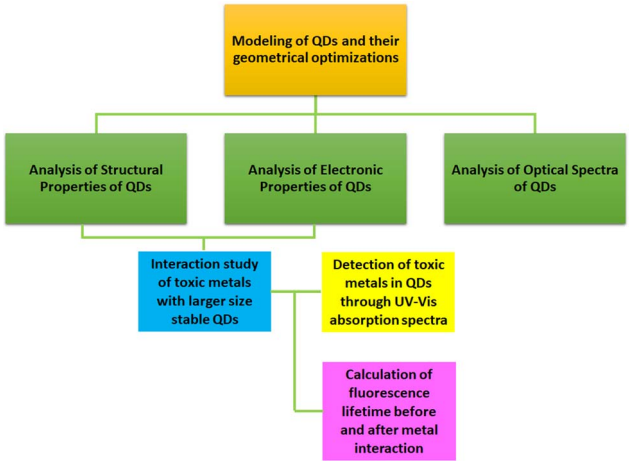

Scheme 1 Flowchart of computational investigations carried out in this work.

computational results obtained through the DFT studies (Scheme 1) will help the experimentalists design engineered QDs as quantum optical sensors for selective detection of toxic elements in drinking water.

2. Computational details

All calculations were carried out using the quantum chemical DFT package Gaussian16 with the Becke-3 parameter-Lee–Yang–Parr (B3LYP) exchange-correlation functional and 6-311G** (d,p)/Los Alamos National Laboratory 2 double-ζ (LANL2DZ) basis sets.[38] Pristine, B/N/S CQDs and BNQDs were modelled and optimized to their ground state. All the systems were passivated with hydrogen (H) atoms to account for stability. Table 1 provides the list of 44 different structures along with the number of H, carbon (C), B, N, and S atoms. The optimized structures of all QDs are given in Fig. 1.

The formation energy of a QD was calculated using the following formula:

$$E_{\text{form}} = [E_{\text{QD}} - (n_x \times E_x + n_y \times E_y + n_z \times E_z)]/N \quad (1)$$

where E_{form} is the formation energy of the QD, E_{QD} is the total energy of the QD, 'n_x' represents either the number of carbon atoms or the number of B atoms, 'n_y' represents either the number of N atoms or S atoms or the number of metals, 'n_z' denotes the number of H atoms and 'N' is the total number of atoms contained in the quantum dot. In addition, we analyzed the HOMO, LUMO, and electrostatic potential (ESP) plots for all the systems.

Further, interactions between the QDs and toxic metals (As, Co, Ni, Cu, and Pb) were examined. The adsorption energy of metals with QDs was calculated using the following formula:

$$E_{\text{adsorption energy}} = E_{\text{complex}} - E_{\text{QD}} - E_{\text{metal}} \quad (2)$$

where E_{complex} is the total energy of a complex made up of QDs and metal, and E_{QD} and E_{metal} are the total energies of QDs and metal, respectively.

Time-dependent DFT (TD-DFT) calculations were performed for all QDs to obtain UV-vis absorption. Moreover, Raman spectra were recorded for all QDs. Similar calculations were performed during metal interaction studies with selected QDs in both gas and water phases to obtain the UV-vis absorption spectra. The fluorescence lifetime calculation was carried out using the following formula:[39]

$$\tau = (1.5 \times 10^4) \frac{{\lambda_{\text{ba}}}^2}{n\left(\frac{n^2+2}{3}\right)^2} \frac{g_b}{g_a} \frac{1}{f} \quad (3)$$

where τ is the lifetime, n is the refractive index, and λ_{ba} is the wavelength between the excited state b and ground state a. g_b and g_a are the degeneracies associated with the excited state and ground state and f is the oscillator strength. Here we take, $g_a = 1$, $g_a = g_b$, and $n = 1.33$ (refractive index of water). Quantitatively, the percentage of change in the intensity of UV-vis absorption spectra after metal adsorption was calculated using the following formula:

$$\text{Change} = \left|\frac{(I_0 - I)}{I_0}\right| \times 100\% \quad (4)$$

where I_0, and I are the intensities of the absorption peaks of QDs in the absence and presence of metals.

3. Results and discussion

3.1 Structural properties

3.1.1 Pristine CQDs. In the optimized pristine CQDs, the bond lengths between C–H bonds (1.08 Å), C–C bonds at edges (1.39 Å), and inner surface (1.43 Å) are constant. The obtained bond lengths of the inner C–C bonds and C–H bonds are close to the previously reported values.[40] The bond angle between carbon atoms is around 120°, and the value remains constant in all systems. Additionally, the planarity of the structures increases with the increase in the size of CQDs. In rectangular CQDs, the number of π-conjugated rings varied from 4 to 9. Accordingly, their length varied from 7.38 Å to 12.29 Å. In circular CQDs, the numbers of π-conjugated rings considered in this study are 7 and 19. The structures of circular CQDs are more planar than those of the rectangular CQDs. Upon increasing the size of the circular CQD, the number of atoms becomes doubled with the diameter ranging from 7.36 Å to 12.30 Å. Triangular CQDs with 3, 10, and 15 π-conjugated rings are considered and their size varies from 4.90 Å to 12.30 Å.

3.1.2 B/N/S-doped CQDs. In B-doped CQDs, the optimized structures show changes in the C–C–C bond angle of about 1° with respect to the pristine rectangular CQDs. The C–B–C bond angle changes with the increase in the size of B-doped CQDs. The optimized C–B bond length is 1.50 Å, which is in a comparable range with B-doped graphenes.[41] B doping leads to a decrease in planarity when compared to pristine CQDs. The optimized bond lengths of the C–C bonds at the inner surface of B-doped CQDs remain the same (1.42 Å), and vary at the edges. The length of the B-doped rectangular CQDs is in the range of 7.39 to 12.32 Å. The diameter of B-doped circular CQDs varies

Table 1 Details of the modelled QDs

CQDs		B/N/S doped CQDs		BNQDs	
Systems	Total no. of atoms	Systems	Total no. of atoms	Systems	Total no. of atoms
Rectangular		**Rectangular**		**Rectangular**	
$H_{11}C_{17}$	28	$H_{11}C_{16}B$	28	$B_{11}N_{17}$	28
$H_{11}C_{19}$	30	$H_{11}C_{18}B$	30	$B_{11}N_{19}$	30
$H_{13}C_{23}$	36	$H_{13}C_{22}B$	36	$B_{13}N_{23}$	36
$H_{13}C_{25}$	38	$H_{13}C_{24}B$	38	$B_{13}N_{25}$	38
$H_{15}C_{29}$	44	$H_{15}C_{28}B$	44	$B_{15}N_{29}$	44
$H_{15}C_{31}$	46	$H_{15}C_{30}B$	46	$B_{15}N_{31}$	46
Circular		$H_{11}C_{16}N$	28	**Circular**	
$H_{12}C_{24}$	36	$H_{11}C_{18}N$	30	$B_{12}N_{24}$	36
$H_{18}C_{54}$	72	$H_{13}C_{22}N$	36	$B_{18}N_{54}$	72
Triangular		$H_{13}C_{24}N$	38	**Triangular**	
H_9C_{13}	22	$H_{15}C_{28}N$	44	B_9N_{13}	22
$H_{15}C_{33}$	48	$H_{15}C_{30}N$	46	$B_{15}N_{33}$	48
$H_{18}C_{46}$	64	$H_{11}C_{16}S$	28	$B_{18}N_{46}$	64
		$H_{11}C_{18}S$	30		
		$H_{13}C_{22}S$	36		
		$H_{13}C_{24}S$	38		
		$H_{15}C_{28}S$	44		
		$H_{15}C_{30}S$	46		

from 7.43 to 12.33 Å. The size of B-doped triangular CQDs is in the range of 4.98 to 12.38 Å.

In N-doped CQDs, the relaxed structures show that the C–C–C and C–N–C bond angles are about 120°, with the increase in size. The optimized C–N bond length is 1.40 Å, and it is similar to N-doped graphenes.[42] The optimized bond length of C–C bonds at the inner surface of the N-doped CQD remains the same (1.42 Å) and varies at the edges. In N-doped rectangular CQDs, planarity varies with the size in a lesser magnitude. Their length varies from 7.32 Å to 12.27 Å. In N-doped circular CQDs, the diameter is in the range of 7.32 Å to 12.33 Å. In N-doped triangular CQDs, the optimized bond lengths of C–C bonds at the edges and inner surface of CQDs are 1.38 Å and 1.41 Å, respectively. The size of triangular N-doped CQDs is in the range of 4.86 Å to 12.27 Å.

In S-doped CQDs, due to the larger radius of the S atom, it protrudes out of the plane. In sulphur-doped circular and triangular CQDs, the relaxed structure shows variation in C–C–C (117.64° to 124.82°) and C–S–C (101.67° to 120.33°) bond angles with the increase in size. The optimized bond length of the C–S bond varies from 1.64 to 1.78 Å with the change in the size of S-doped CQDs. The C–S bond length agrees with the previous observations made by Zhao and Ma on sulphur-doped graphenes.[43] The length of S-doped rectangular CQDs is in the range of 7.59 to 12.52 Å. The diameter of S-doped circular CQDs is in the range of 7.37 to 12.46 Å. In triangular S-doped CQDs, the optimized bond lengths of carbon C–C at the edges and inner surface of CQDs are 1.39 and 1.41 Å respectively. Their size is in the range of 5.19 to 12.49 Å.

3.1.3 BNQDs. In BNQDs, the optimized B–N–B and N–B–N bond angles are 120° and show negligible changes when compared to the pristine CQDs. The optimized boron–nitrogen (B–N), boron–hydrogen (B–H), and nitrogen–hydrogen (N–H) bond lengths are 1.45, 1.19, and 1.01 Å, respectively. The attained bond lengths are in line with the previously reported values.[44] Negligible changes in the bond lengths of B–N, B–H, and N–H are observed with the increase in the size of BNQDs. Since the B–N bond length is higher than that of the C–C bond length, the size of BNQDs is larger than that of their CQD counterparts. In BNQDs with the rectangular morphology, the number of hexagonal lattices varied from 4 to 9. The length of rectangular BNQD is in the range from 7.48 Å to 12.53 Å. In circular BNQDs, the number of hexagonal lattices considered in this study is 7 and 19. The size of the circular BNQDs varies from 7.50 Å to 12.52 Å. BNQDs with the triangular morphology consisting of 3, 10, and 15 hexagonal lattices are considered and their size varies from 4.97 Å to 12.55 Å.

3.1.4 Formation energy analysis

3.1.4.1 Pristine CQDs. The formation energy of pristine CQDs is negative, and it implies that they are energetically stable. A similar kind of observation has been reported by Yamijala *et al.*, for graphene QDs.[45] The formation energy of rectangular, circular, and triangular CQDs varies from −6.10 eV to −5.50 eV, −6.80 eV to −6.06 eV, and −6.46 eV to −5.35 eV, respectively. In comparison, it can be understood that circular CQDs are more stable, energetically. Though rectangular $H_{13}C_{23}$ CQDs and circular $H_{12}C_{24}$ CQDs have almost the same number of atoms, there is a significant difference in their formation energy (−5.79 and −6.06 eV). At this juncture, one can understand that the morphology of the CQDs determines the stability too. Interestingly, there are many experimental reports on circular CQDs that have been investigated by atomic force microscopy and transmission electron microscopy characterization techniques.[46]

3.1.4.2 B/N/S-doped CQDs. The formation energy of B-doped rectangular, circular, and triangular CQDs varies in the range of −6.01 eV to −5.36 eV, −6.74 eV to −5.08 eV, and −6.41 to −5.17 eV, respectively. Circular $H_{12}C_{23}B$ CQDs show

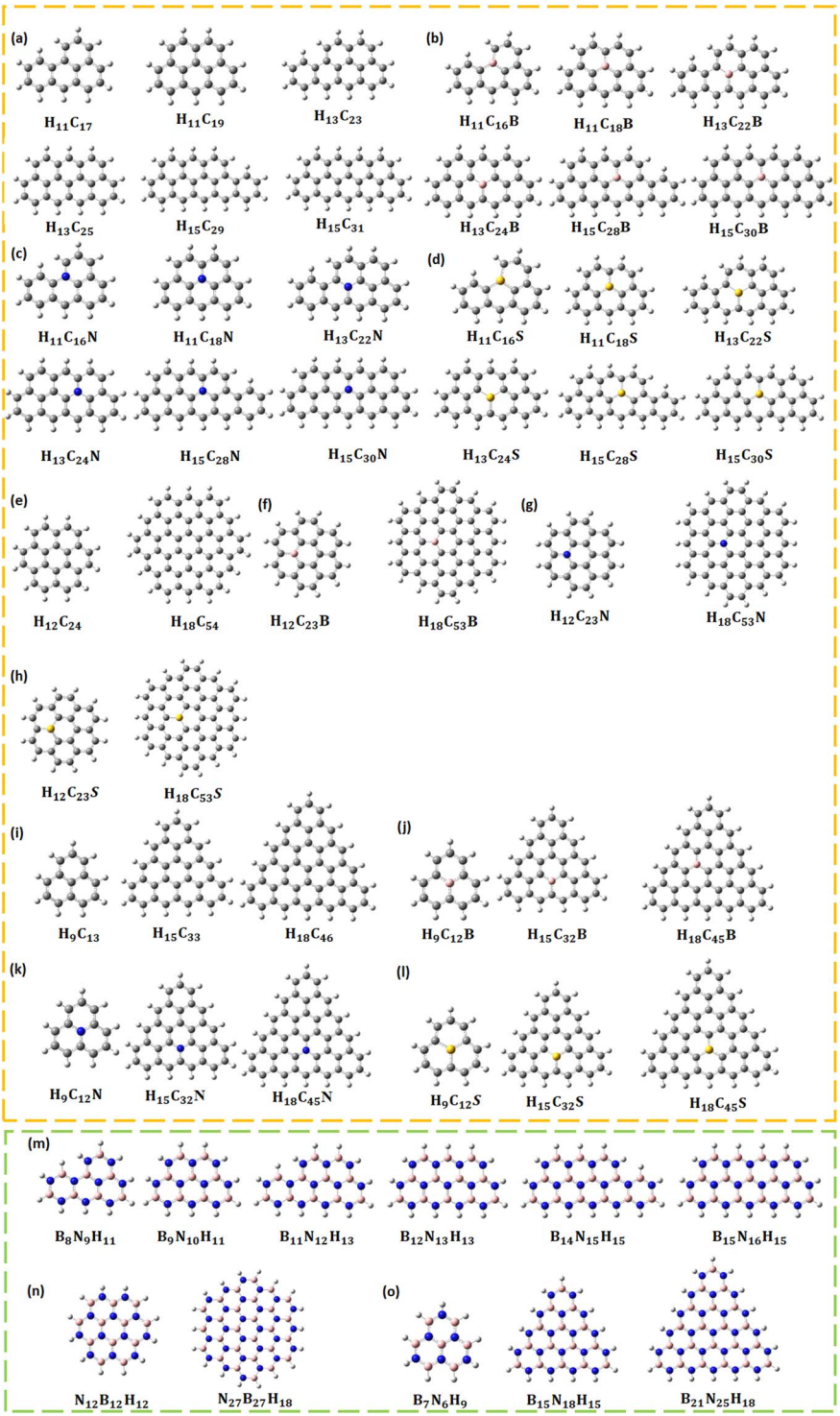

Fig. 1 Optimized structures: rectangular (a) CQDs, (b) B-doped CQDs, (c) N-doped CQDs, and (d) S-doped CQDs; circular (e) CQDs, (f) B-doped CQDs, (g) N-doped CQDs, and (h) S-doped CQDs; triangular (i) CQDs, (j) B-doped CQDs, (k) N-doped CQDs, and (l) S-doped CQDs; (m) rectangular BNQDs, (n) circular BNQDs, and (o) triangular BNQDs (white, grey, pink, blue, and yellow balls represent hydrogen, carbon, boron, nitrogen, and sulphur atoms, respectively).

a maximum change in their formation energy (−0.98 eV) compared to their pristine systems, whereas triangular $H_{18}C_{46}B$ CQDs show a minimum change in their formation energy (−0.05 eV). The formation energy range of N-doped rectangular CQDs is similar to that of B-doped rectangular CQDs (−6.01 eV to −5.41 eV). The range of formation energy of N-doped circular and triangular CQD varies from −6.76 eV to −5.81 eV and −6.44 eV to −5.25 eV, respectively. Circular $H_{12}C_{23}N$ CQDs show a maximum change in their formation energy (−0.25 eV) compared to their pristine forms, whereas triangular $H_{18}C_{45}N$

CQDs show a minimum change in their formation energy (−0.02 eV). The formation energy of rectangular, circular, and triangular S-doped CQDs varies in the range of −5.86 to −5.15 eV, −5.42 to −4.74 eV, and −5.14 to −4.90 eV, respectively. Circular $H_{18}C_{53}S$ shows a maximum change in its formation energy (−1.39 eV) compared to the pristine circular CQD ($H_{18}C_{54}$) and triangular $H_9C_{12}S$ shows a minimum change in its formation energy (−0.46 eV) compared to its pristine counterpart. The formation energy range of all B/N/S-doped CQDs is negative, hence they are stable.

3.1.4.3 BNQDs. Similar to CQDs, the formation energy values of all BNQDs with different morphologies are negative and they are energetically stable. This is in line with the previous report.[47] The range of formation energy of rectangular, circular, and triangular BNQDs is −5.36 eV to −4.84 eV, −5.96 eV to −5.27 eV, and −5.79 to −4.58 eV, respectively. Experimentally, Sert *et al.*, have reported on the synthesis of BNQDs with circular morphology.[48]

3.2 Electronic properties

3.2.1 ESP analysis. ESP plot is an important tool to identify the electron-deficient and electron-excess regions in a molecule. Fig. S1† consists of the ESP plots of all QDs. In pristine CQDs, high- and low-electron density regions are indicated by red and blue colours, respectively. The high and uniform electron density in the carbon region is due to the presence of delocalized π electrons. The low electron density is observed near the hydrogen-bonded region. Similar results have been reported by Jiang *et al.*, for carbon structures such as graphenes.[49] B doping has led to a change in the hybridization of carbon atoms ($sp^2 \rightarrow sp^3$) which significantly has modulated the electronic distribution on the surface of the doped CQDs. As a result, there is a non-uniform electron density. The doping has reduced the surrounding electrostatic charge over B, resulting in an electron-rich red region over the doped area. Hadki *et al.*, have reported a similar observation for boron-doped reduced graphene oxide.[50] N and S dopants have reduced the electron density around the carbon atoms near them. The changes are indicated by the presence of less reddish and more bluish regions on the inner surface of N/S-doped CQDs. The charge transfer between carbon and nitrogen/sulphur has led to this electron density variation in the ESP plot. Both N and S in the CQDs act as an electron-deficient region. Our observations are in line with earlier reports.[50,51] In BNQDs, there is a presence of neutral region around B and N in the inner surface and less electron density at the hydrogen in the ESP plot. Hence, the reactive zones of the BNQDs are located on the B–H bonds.[52] A similar ESP plot was obtained by Talaei *et al.*, for h-BNQDs with circular morphology.[53]

3.2.2 Frontier molecular orbitals analysis

3.2.2.1 Pristine CQDs. The analysis of frontier molecular orbitals (FMOs) such as HOMO and LUMO followed by the calculated energy gap helps determine the chemical stability of a system. The system having the highest energy gap is more chemically stable. The pictorial illustration of the HOMO–LUMO analysis plots of all QD systems is given in Fig. S2.† Due to the presence of unpaired electrons in some of the QDs, the spin is in a doublet state which causes the FMO to split into alpha and beta molecular orbitals.[54,55] In rectangular CQDs, the spin of rectangular CQD is in a doublet state which causes the frontier orbitals to split into alpha and beta molecular orbitals having two different energy gaps. This kind of observation was earlier reported for an organic molecule.[56] The energy gap decreases with the increase in the size of rectangular CQDs due to the quantum confinement effect. This observation agrees with the previous report on graphene QDs.[57] The energy gap of alpha molecular orbitals varies from 2.29 ($H_{15}C_{31}$) to 3.24 eV ($H_{11}C_{17}$). The increasing order of stability of rectangular CQDs for alpha molecular orbitals based on the energy gap is as follows:

$$H_{15}C_{31} < H_{15}C_{29} < H_{13}C_{25} < H_{13}C_{23} < H_{11}C_{19} < H_{11}C_{17}$$

The energy gap of beta molecular orbitals varies from 2.21 to 3.33 eV. The same trend was observed for beta molecular orbitals too.

The energy gap of circular CQDs decreases with the increase in diameter. A similar observation has been reported by Kateris *et al.*, for polycyclic aromatic hydrocarbons.[58] Smaller sized circular CQDs ($H_{12}C_{24}$) have the highest energy gap of 4.00 eV and larger sized circular CQDs ($H_{18}C_{54}$) have the lowest energy gap of 2.81 eV. This observation is in line with the previously reported values for similar systems investigated by Masfioui *et al.*, using the B3LYP functional and a 6-31 g (d) basis set.[59] In triangular CQDs, the spin of H_9C_{13} and $H_{15}C_{33}$ is in a doublet state. Hence, the frontier orbitals to split into alpha and beta molecular orbitals have two different energy gaps. Similar to rectangular and circular CQDs, the energy gap decreases with the increase in size in triangular CQDs. The energy gap of triangular CQDs varies from 0.30 ($H_{18}C_{46}$) to 4.04 (H_9C_{13}) eV. The increasing order of stability of triangular CQDs based on the energy gap is as follows:

$$H_{18}C_{46} < H_{15}C_{33} < H_9C_{13e}$$

Overall, based on the energy gap, it can be concluded that circular CQDs are more chemically stable than triangular and rectangular CQDs. Interestingly, most of the CQDs which are experimentally synthesized have the circular morphology.[13]

3.2.2.2 B/N/S-doped CQDs. The doping of B/N/S on the surface of CQDs leads to the creation of additional energy levels between π (bonding) and π* (antibonding) molecular orbitals of the C atom. Hence, the variations in the HOMO and LUMO values are observed. Conversely, the energy gap gets changed too. A similar kind of observation has been made by Feng *et al.*, for B-doped graphene dots.[60]

3.2.2.2.1 B-doped CQDs. All rectangular, circular, and triangular B-doped CQDs have a lesser energy gap than that of their pristine counterparts. The energy gap of rectangular B-doped CQDs is in the range of 1.25 eV to 1.93 eV. The increasing order of stability based on the energy gap is as follows:

$H_{13}C_{24}B < H_{15}C_{28}B < H_{15}C_{30}B < H_{13}C_{22}B < H_{11}C_{16}B < H_{11}C_{18}B$

In circular B-doped CQDs, the doping leads to a decrease in the energy gap. A similar observation was made by Sun *et al.*, for B-substituted coronene. They have reported that the resulting LUMO level mainly originates from the C and H atoms instead of the B atoms leading to a change in the energy gap.[61] The energy gap of alpha and beta molecular orbitals varies from 2.63 eV to 3.87 eV and 1.15 to 1.70 eV, respectively. The energy gap of B-doped triangular CQDs varies from 0.45 to 1.97 eV. Here, the increasing order of stability is as follows:

$$H_{15}C_{32}B < H_{18}C_{45}B < H_9C_{12}B$$

3.2.2.2.2 N-doped CQDs. The energy gap has decreased in all N-doped rectangular, circular, and triangular CQDs compared to the bare CQDs. The energy gap of N-doped rectangular CQDs varies from 1.36 to 1.99 eV. The increasing order of chemical stability based on the energy gap for N-doped rectangular CQDs is as follows:

$$H_{15}C_{28}N < H_{15}C_{30}N < H_{13}C_{24}N < H_{13}C_{22}N < H_{11}C_{16}N < H_{11}C_{18}N$$

In N-doped circular CQDs, the spin of $H_{12}C_{23}N$ and $H_{18}C_{53}N$ is in a doublet state, and hence, the frontier orbitals split into alpha and beta molecular orbitals. The energy gap of alpha and beta molecular orbitals varies from 1.16 eV to 1.67 eV and 2.68 eV to 3.88 eV. The energy gap of N-doped triangular CQDs varies from 0.39 to 2.20 eV. Only $H_{18}C_{45}N$ is in a doublet state, and the energy gap for split alpha and beta molecular orbitals are 1.24 and 0.98 eV, respectively.

3.2.2.2.3 S-doped CQD. All S-doped rectangular CQDs are in a doublet state. The energy gap of alpha and beta molecular orbitals varies from 0.34 eV to 2.89 eV and 1.21 eV to 1.70 eV, respectively. Based on the energy gap, the increasing order of stability for alpha molecular orbitals is as follows:

$$H_{11}C_{18}S < H_{15}C_{30}S < H_{15}C_{28}S < H_{13}C_{22}S < H_{13}C_{24}S < H_{11}C_{16}S$$

Similarly, the increasing order of stability for beta molecular orbitals is as follows:

$$H_{15}C_{28}S < H_{15}C_{30}S < H_{13}C_{24}S < H_{13}C_{22}S < H_{11}C_{16}S < H_{11}C_{18}S$$

In S-doped circular CQDs, S doping has led to a decrement in the energy gap. The energy gap of S-doped circular CQDs varies from 1.18 ($H_{12}C_{23}S$) to 2.67 ($H_{18}C_{53}S$) eV and those values are less than those of the pristine counterparts. In S-doped triangular CQDs, the spin of $H_9C_{12}S$ and $H_{15}C_{32}S$ is in a doublet state, so frontier orbitals split into alpha and beta molecular orbitals. The energy gap of alpha and beta molecular orbitals varies from 2.25 eV to 2.96 eV and 0.93 eV to 1.37 eV. The energy gap of S-doped triangular CQDs varies from 0.25 eV to 2.96 eV. Collectively, we can observe that B/N/S-doped circular CQDs are more chemically stable than the B/N/S-doped rectangular and triangular CQDs.

3.2.2.6 BNQDs. In rectangular BNQDs, there is a decrease in the energy gap with the increase in the size of the systems. However, the reduction is very minimal when compared to the CQDs. A similar observation has been highlighted by Guerra *et al.*, for hexagonal BN nanoflakes.[62] The energy gap of rectangular BNQDs lies between 6.06 and 6.16 eV. Based on the obtained energy gap, it is understood that the stability of BNQD is very high compared to pristine and B/N/S-doped CQDs. The increasing order of stability for rectangular BNQDs based on the energy gap is as follows:

$$B_{14}N_{15}H_{15} < B_{15}N_{16}H_{15} < B_{11}N_{12}H_{13} < B_{12}N_{13}H_{13} < B_8N_9H_{11} < B_9N_{10}H_{11}$$

A similar trend is exhibited by circular BNQDs with the increase in size. It is in line with the observations of Shayeganfar *et al.*, on functionalized BNQDs having circular shapes.[63] The energy gap of circular BNQDs varies from 6.27 eV to 6.64 eV. $B_{12}N_{12}H_{12}$ and $B_{27}N_{27}H_{18}$ have the highest and lowest energy gaps, respectively. In triangular BNQDs too, a decrease in the energy gap due to the increase in the number of atoms and size of BNQD is observed. The energy gap of triangular BNQDs varies from 5.77 eV to 7.11 eV. The increasing order of stability for triangular BNQDs based on energy gap is as follows:

$$B_{21}N_{25}H_{18} < B_{15}N_{18}H_{15} < B_7N_6H_9$$

Viana *et al.*, have observed similar results for BN nanoflakes having different morphologies.[64] Overall, BNQDs are more stable than their corresponding CQDs of any morphology.

3.3 Optical properties

3.3.1 UV-visible absorption spectra analysis. In our investigations, we have obtained the UV-vis absorption spectra of all QDs in water. In common, due to the reduction in the energy gap with the increase in the QD sizes, we observed a red shift in the characteristic peaks of all QDs. This is due to the quantum confinement effect. A similar observation has been reported by Zhang *et al.*, for graphene QDs of different sizes.[65] The UV-vis absorption spectra of QDs are shown in Fig. 2.

3.3.1.1 Pristine CQDs. Two characteristic peaks have been observed in CQDs (rectangular, circular and triangular). They occur due to π (bonding orbital)-to-π* (antibonding orbital) and n (non-bonding orbital)-to-π* transition, as reported by Zhang *et al.*, for graphene QDs.[66] The π-to-π* transition occurs in the wavelength range of 228–312 nm, 211–284 nm, and 232–408 nm for rectangular, circular and triangular CQDs, respectively. This transition is due to the presence of aromatic sp^2 (C=C) domains.[67] Similarly, n-to-π* transition is observed in the wavelength range of 358–391 nm, 312–447 nm, and 343–408 nm for rectangular, circular and triangular CQDs, respectively.

3.3.1.2 B/N/S-doped CQDs

3.3.1.2.1 B-doped CQDs. In B-doped rectangular CQDs, we notice three characteristic peaks. One of the peaks is due to π-to-π* transition and the other two peaks are due to n-to-π* transition. This observation matches with the report of Fan *et al.*, on B-doped graphene quantum dots.[68] The π-to-π* transition in the wavelength range of 222–308 nm is due to the presence of aromatic sp^2 (C=C) domains. The n-to-π* transition in the wavelength range of 290–500 nm is due to the C–B bonds.[69] In B-doped circular CQDs, there is only one characteristic peak in the wavelength range of 299–455 nm. The wavelength shift is more in B-doped circular CQDs than in pristine circular CQDs. Saha and Bhattacharyya have made a similar observation in B-doped coronene.[70] Two characteristic peaks except for $H_{18}C_{45}B$ are detected in the wavelength range of 191–403 nm. As noted in other QDs, the π-to-π* transition in the wavelength range of 191–284 nm is due to the presence of aromatic sp^2 (C=C) domains. Moreover, the n-to-π* transition has occurred in the wavelength range of 357–404 nm due to the C–B bonds.

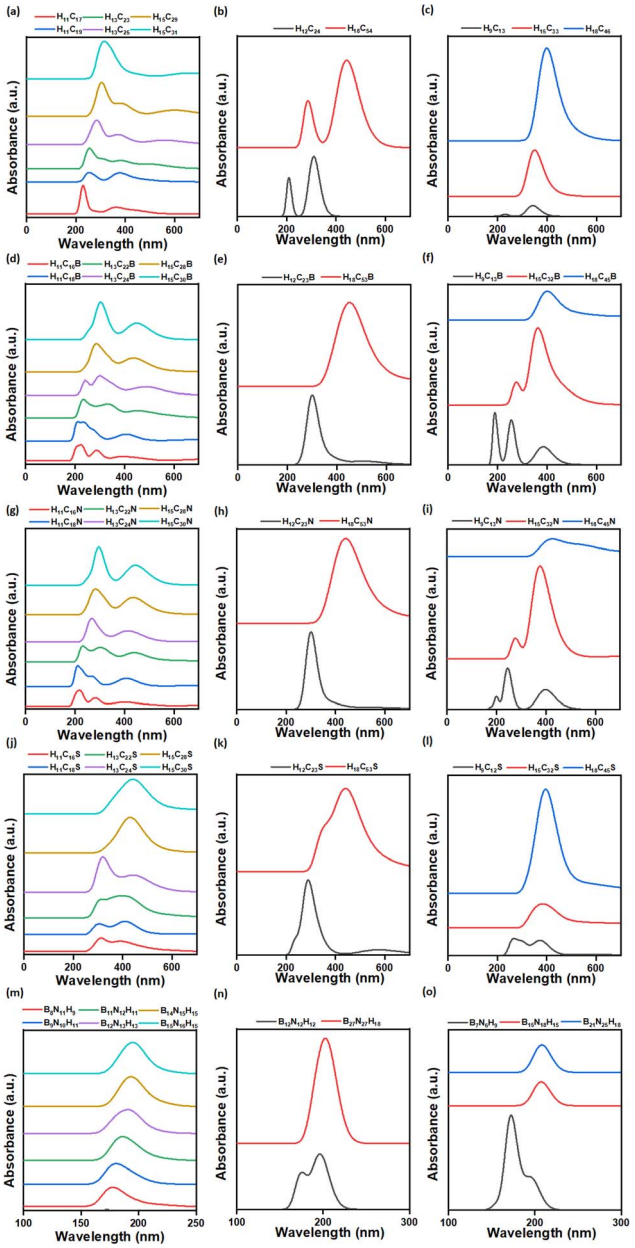

Fig. 2 UV-vis absorption spectra of (a) rectangular CQDs, (b) circular CQDs, (c) triangular CQDs, (d) rectangular B-doped CQDs (e) circular B-doped CQDs, (f) triangular B-doped CQDs, (g) rectangular N-doped CQDs, (h) circular N-doped CQDs, (i) triangular N-doped CQDs, (j) rectangular S-doped CQDs, (k) circular S-doped CQDs, (l) triangular S-doped CQDs, (m) rectangular BNQDs, (n) circular BNQDs, and (o) triangular BNQDs.

3.3.1.2.2 N-doped CQDs. The N doping in rectangular CQDs gives rise to 2 important characteristic peaks. They are due to π-to-π* and n-to-π* transitions. A similar kind of remark has been made by Hasibuan *et al.*, in their research work on N-doped carbon dots.[71] Here too, the π-to-π* transition occurs in the wavelength range of 214–296 nm due to the presence of aromatic sp^2 (C=C) domains. The n-to-π* transition is observed in the wavelength region below 500 nm, and this is due to the transition between the non-bonding orbital of C=N and the antibonding orbital (π*) of carbon. In N-doped circular CQDs, only one characteristic peak in the wavelength range of 302 to 442 nm, corresponding to the n-to-π* transition, is observed. This is because of the n-to-π* transition between the non-bonding orbital of C=N and the antibonding orbital (π*) of carbon. In triangular N-doped CQDs, two characteristic peaks except for $H_{18}C_{45}N$ have been noticed. Similar to previous cases, the π-to-π* transition happens in the wavelength range of 204–273 nm, because of the presence of aromatic sp^2 (C=C) domains. Parallelly, the n-to-π* transition occurs in the wavelength region (382 to 423 nm) below 500 nm due to the non-bonding orbital of C=N and the antibonding orbital (π*) of the C atom.

3.3.1.2.3 S-doped CQDs. The UV-vis absorption spectrum of S-doped rectangular CQDs in water gives rise to characteristic peaks, which are due to π-to-π* and n-to-π* transitions. A similar kind of observation was reported by Wu *et al.*, for S-doped CQDs.[72] The occurrence of π-to-π* transition was observed in the wavelength range of 304–320 nm, which is due to the presence of aromatic sp^2 (C=C) domains. The occurrence of n-to-π* transition was observed in the wavelength region below 500 nm. With the increase in the size of rectangular S-doped CQDs, the red shift was observed in the UV absorption spectrum as the absorption peaks shifted towards a higher wavelength.[65] S-doped circular CQDs give rise to characteristic peaks due to π-to-π* and n-to-π* transitions, as highlighted by Wu *et al.*, in S-doped CQDs.[72] The π-to-π* transition was observed for $H_{12}C_{23}S$ at a wavelength below 300 nm and it is due to the presence of aromatic sp^2 (C=C) domains. Here, n-to-π* transition is observed for all circular S-doped CQDs in the wavelength region below 500 nm. With the increase in the size of circular S-doped CQDs, the red shift is observed in the UV absorption spectrum. In triangular S-doped CQDs, two characteristic peaks were obtained in the wavelength range of 268–400 nm. The π-to-π* transition was observed for $H_9C_{12}S$ at a wavelength below 300 nm due to the presence of aromatic sp^2 (C=C) domains. The n-to-π* transition was observed for all

triangular S-doped CQDs in the wavelength region below 400 nm. Similar to S-doped circular CQDs, the red shift is observed in S-doped triangular CQDs with the increase in size.

3.3.1.3 BNQDs. In the UV-vis absorption spectra of all rectangular, circular, and triangular BNQDs, a single absorption peak is observed in the wavelength ranges of 178–196 nm, 176 to 202 nm, and 174 to 210 nm, respectively. A similar kind of observation was made by Sert *et al.*, for BNQDs.[48]

3.3.2 Raman spectra analysis

3.3.2.1 Pristine CQDs. Raman spectroscopy is a non-destructive tool used to investigate the degree of structural disorder in the carbon matrix occurring due to doping, vacancy, and point defects, both quantitatively and qualitatively.[73] Raman spectrum is classified into two zones: one of them corresponds to the spectral range of 900–1900 cm^{-1} (first-order spectrum) and the other zone to 2500–3300 cm^{-1} (second-order spectrum).[74] The typical features of Raman spectra of carbonaceous materials are the D (disorder) band, which arises due to the presence of defects in carbon, the G (graphitic order) band arising from the stretching of the C–C bond, the 2D (D peak overtone) band arising due to in-plane vibrations, D + G band arising due to the combination of overtone, D′ which is a phonon mode arising due to defects, and 2G which is a second-order mode appearing at higher frequencies.[68]

In the Raman spectra of pristine CQDs with various morphologies such as rectangular, circular, and triangular, the spectral range from 0 to 3500 cm^{-1} is considered (Fig. S3†). As the size of CQD increases, the intensity of the bands lying in the spectral range from 1300 to 1600 cm^{-1} and beyond 3100 cm^{-1} also increases. The Raman spectra of pristine CQDs show second-order modes (2G) around 3178–3185 cm^{-1}. This arises due to the C–H vibrations of CQD. The intensity of the 2G band increases and becomes well defined with the increase in the size of the CQDs. Dervishi *et al.*, have reported a similar observation in graphene QDs.[75] The D and G characteristic bands appear in the wavelength range of 1344 to 1371 cm^{-1} and 1571 to 1651 cm^{-1}, respectively. The presence of D and G bands in circular CQDs ($C_{24}H_{12}$, and $C_{54}H_{18}$), agrees with the previous observation made by Shtepliuk *et al.*, for graphene QDs ($C_{24}H_{12}$).[76]

3.3.2.2 B-doped CQDs. In the B-doped CQDs too, with the increase in the size, the intensity of bands lying in the wavelength region of 1000 to 1600 cm^{-1} and beyond 3100 cm^{-1} increases. There is an appearance of second-order modes (2G) in the wavelength range of 3000 to 3200 cm^{-1}, as highlighted by Venkatesan *et al.*, for B-doped graphenes.[77] The intensity of 2G bands becomes well defined with the increase in the size of B-doped CQDs.

In B-doped rectangular CQDs, the D and G bands appear in the spectral range of 1365–1386 cm^{-1} and 1575–1603 cm^{-1}, respectively. These are in line with previously reported observations.[78–80] In $H_{11}C_{16}B$, $H_{13}C_{24}B$, and $H_{15}C_{28}B$ systems, the intensity of the peak appearing at 1638 cm^{-1} increases. In all B-doped rectangular CQDs, intense peaks were obtained between 1300 and 1600 cm^{-1}. This is in line with the report of Zhang *et al.*, on B-doped graphene QDs.[81] The appearance of new bands was observed in all B-doped rectangular CQDs in the spectral range of 2947 to 2989 cm^{-1} and at 1806 cm^{-1}. However, the intensity of the bands is low. A similar observation was reported by Kim *et al.*, for B-doped graphenes for the band appearing at 2950 cm^{-1}. This band arises due to a defect and it is attributed to the defect-induced double resonance (D + D′). They originate due to B doping in the CQD.[82] The disappearance of peaks in the spectral range from 1785 to 1799 cm^{-1}, 3360 to 3367 cm^{-1}, and 1806 to 1813 cm^{-1} was observed in $H_{11}C_{18}B$, $H_{13}C_{22}B$, and $H_{13}C_{24}B$, respectively.

In B-doped circular CQDs, the D band appears at 1372 cm^{-1} and the G band appears in the wavelength range of 1533–1582 cm^{-1}, respectively. The appearance of new peaks in the spectral range of 2986 to 2989 cm^{-1} was observed in the Raman spectrum of $H_{12}C_{23}B$, and $H_{18}C_{53}B$. The disappearance of peaks in the spectral range of 1813 to 1820 cm^{-1} was observed in $H_{18}C_{53}B$ compared to the Raman spectrum of $H_{18}C_{54}$ and also at 1806 cm^{-1} for $H_{12}C_{23}B$ when compared to the Raman spectrum of $H_{12}C_{24}$.

In B-doped triangular CQDs, the D and G bands appear in the spectral range of 1302–1386 cm^{-1} and 1547–1596 cm^{-1}, respectively. These are in line with the earlier observations.[78,79] The appearance of new peaks in the spectral range from 2954 to 2996 cm^{-1} was observed in the Raman spectrum of $H_9C_{12}B$, and $H_{15}C_{32}B$. These peaks correspond to D + D′ bands, and a similar observation was made by Chesnokov *et al.*, in B-doped graphenes.[80] The disappearance of peaks in the spectral range of 1771 to 1778 cm^{-1} was observed in $H_{18}C_{45}B$ compared to the pristine CQD, $H_{18}C_{46}$.

3.3.2.3 N-doped CQDs. In N-doped CQDs, there is an appearance of second-order modes (2G) in the wavelength range of 3000 to 3200 cm^{-1}. A similar observation was reported by Atchudan *et al.*, for nitrogen-doped CQDs.[83]

In the N-doped rectangular CQDs, the D and G bands appear in the wavelength range of 1372–1393 cm^{-1} and 1610–1652 cm^{-1} respectively. These are in line with the earlier observations made by Liu *et al.*, for N-doped CQDs.[84] The presence of the D′ band at 1624 cm^{-1} in N-doped rectangular CQDs was reported by Zafar *et al.*, for N-doped graphenes too.[85] In all N-doped rectangular CQDs, the band's intensity appearing between 1650 and 1675 cm^{-1} increases. In N-doped rectangular CQDs, there is an appearance of new bands in the spectral range of 1806 to 1827 cm^{-1} and 3300 to 3500 cm^{-1}. The bands at 2996 cm^{-1} in $H_{13}C_{24}N$ and $H_{15}C_{30}N$ have disappeared.

In the Raman spectra of N-doped circular CQDs having various sizes, the D and G bands appear in the spectral range of 1351–1379 cm^{-1} and 1617–1638 cm^{-1}, respectively. A similar observation is made by Ayiania *et al.*, for N-doped coronene.[86] The appearance of new peaks at 1813 cm^{-1} and also in the spectral range of 3339 to 3353 cm^{-1} was observed in the Raman spectrum of $H_{12}C_{23}N$. Similarly, a new peak at 3339 cm^{-1} was observed for $H_{18}C_{53}N$. The peak at 2996 cm^{-1} in $H_{12}C_{23}N$ vanished when compared to the pristine $H_{12}C_{24}$.

In the Raman spectra of N-doped triangular CQDs, the D and G bands appear in the spectral range of 1309–1365 cm^{-1} and 1561–1582 cm^{-1}, respectively. New peaks appeared in the spectral range of 1750 to 1813 cm^{-1} and at 3346 and 3367 cm^{-1}. The peaks at wavelengths 3003 and 3010 cm^{-1} in $H_9C_{12}N$

disappeared when compared to the Raman spectrum of H_9C_{13}. Similarly, the appearance of new peaks at wavelengths 1778, 1785, 3346, and 3353 cm^{-1} was observed in the Raman spectrum of $H_{15}C_{32}N$ compared to the Raman spectrum of $H_{15}C_{33}$. The appearance of new peaks in the spectral range of 1785 to 1869 cm^{-1} and at wavelength 3346 cm^{-1} was observed in the Raman spectrum of $H_{18}C_{45}N$ when compared to pristine $H_{18}C_{46}$.

3.3.2.4 S-doped CQDs. The Raman spectra of the S-doped rectangular CQDs were observed in the spectral range from 0 to 3500 cm^{-1}. The characteristic bands, D and G, appear in the wavelength range of 1344–1358 cm^{-1} and 1533–1624 cm^{-1}, respectively. This agrees with the earlier observations made by Kadian *et al.*, for S-doped graphene QDs.[51] As the size of CQDs increases, the intensity of the bands lying in the spectral range of 300–1800 cm^{-1} and beyond 3100 cm^{-1} also becomes more intense, and the second-order modes (2G) appear in the spectral range of 3178–3192 cm^{-1}. The disappearance of peaks in the wavelength range from 1771 to 1813 cm^{-1} was observed in the Raman spectrum of $H_{11}C_{16}S$, $H_{15}C_{28}S$, and $H_{15}C_{30}S$ and also in the wavelength range of 3360 to 3353 cm^{-1} was observed in the Raman spectrum of $H_{13}C_{22}S$, $H_{13}C_{24}S$, and $H_{15}C_{28}S$. The appearance of peaks in the wavelength range 3367 to 3430 cm^{-1} was observed in the Raman spectrum of $H_{11}C_{16}S$, $H_{13}C_{22}S$ and also at wavelength 2996 cm^{-1} for $H_{11}C_{16}S$, $H_{13}C_{24}S$.

3.3.2.5 BNQDs. In the Raman spectra of BNQDs with various morphologies such as rectangular, circular, and triangular, the spectral range was considered from 200 to 2000 cm^{-1}. In all BNQDs, when the size is increased, the intensity of the bands lying in the spectral range of 1000–1600 cm^{-1} also increases. In all BNQDs of various sizes and morphologies, a characteristic peak with low intensity appears in the wavelength range of 1344 to 1379 cm cm^{-1}. This peak corresponds to the E_{2g} vibration mode due to the stretching of the B–N bond in h-BN, this agrees with the previous observation reported by Ahmad *et al.*, for h-BNQDs.[87]

3.4 Interaction studies of toxic metals with QDs

Larger sized QDs (rectangular $H_{15}C_{31}$, circular $H_{18}C_{54}$, triangular $H_{18}C_{46}$, rectangular $H_{15}C_{30}B/N/S$, rectangular $B_{15}N_{16}H_{15}$, circular $B_{27}N_{27}H_{18}$, and triangular $B_{21}N_{25}H_{18}$) are taken for the toxic metal interaction studies due to their enhanced structural stability. The investigations were carried out in both gas and water phases. After metal adsorption, we can observe changes in the bond lengths, bond angles and planarity in a few of the CQDs and B/N/S-doped CQDs. However, negligible changes are noted in B–N, B–H, and N–H bond lengths, and N–B–N and B–N–B bond angles after metal complexation in BNQDs. Hence, their planarity is preserved even after the metal adsorption. Fig. 3 represents the QD + metal complexes having higher interactions with each other and the rest of them are given in Fig. S4.† The calculated formation energy of metal-adsorbed QDs was found to be negative, implying the formation of structurally stable complexes (Table S1†).

3.4.1 Arsenic. In As-adsorbed pristine CQDs, there is no significant change in the C–C–C bond angles and hence the planarity too. Among them, the triangular CQD ($H_{18}C_{46}$ + As) has the highest adsorption energy (−3.29 eV), suggesting the chemisorption of As on the substrate. Here, the hybridization between the 4p orbitals of As and 2p orbitals of C in the CQD is responsible for the interaction between the former and the latter.[88] Among rectangular CQDs, $H_{15}C_{31}$ + As has the lowest adsorption energy (−0.02 eV), which means it is physisorbed. The lowest adsorption energy (−0.55 eV) of As with circular CQDs ($H_{18}C_{54}$ + As) can be attributed to its high stability.

The As adsorption energies in B/N/S doped CQDs are in the range of −1.27 eV to −3.16 eV, which confirms the chemisorption of As on these systems. The obtained adsorption energy values with $H_{15}C_{30}B$, and $H_{15}C_{30}N$ agree with the previous reports.[89,90] $H_{15}C_{30}S$ has the highest adsorption energy towards As (−3.16 eV) among all other QDs. Due to the strong interaction, the C–S–C bond angle has changed about 20.72°. The planarity of $H_{15}C_{30}S$ + As gets distorted by 38.12°. The interaction distance between As and S (2.20 Å) closely agrees with the bond length As–S bond of Arsenopyrite.[91] In all BNQDs, the As adsorption energies are nearly the same (−1.03 to −1.06 eV) suggesting chemisorption. The planarity of $B_{15}N_{16}H_{15}$ + As gets reduced on As interaction and the highest change occurs by about 6.90°.

3.4.2 Cobalt. After the interaction of Co with pristine CQDs, there is no appreciable change in the C–C–C bond angle and planarity. The interaction of Co leads to an increase in the diameter of the circular and triangular CQDs only. The adsorption energy ranges from −1.32 to 0.39 eV and occurs at an interaction distance (2.02 to 2.83 Å) for the adsorption of Co onto CQDs. The rectangular CQD ($H_{13}C_{25}$ + Co), circular CQD ($H_{18}C_{54}$ + Co), and triangular CQD ($H_{18}C_{46}$ + Co) have negative adsorption energies, which suggests that the adsorption of Co with CQDs is possible. For systems such as rectangular CQDs ($H_{15}C_{31}$ + Co), the adsorption energy value is positive, which implies that the adsorption of Co on these systems does not occur spontaneously. The triangular CQD with Co ($H_{18}C_{46}$ + Co) has the highest adsorption energy (−1.31 eV), which suggests that Co is chemisorbed on CQDs. The interaction between Co and CQDs is due to the hybridization between the 3d orbitals of Co and the π (p) orbitals of C of CQDs, and a similar observation was made by Rudenko *et al.*, for Co interaction with graphenes.[92]

The interaction of Co with B/N/S-doped rectangular CQDs causes no appreciable change in the C–C–C bond angle and C–(B/N)–C bond angle, except C–S–C. The C–S–C bond angle has changed by 14.46°. The planarity gets disturbed on this interaction, and the planarity of $H_{15}C_{30}S$ + Co (35.32°) gets affected more. The Co-metal shows good bond formation with S of $H_{15}C_{30}S$ at an interaction distance of 2.04 Å, which matches the bond length of the cobalt–sulphide system.[93] Similarly, the diameter of $H_{15}C_{30}S$ + Co has varied (0.35 Å) much from its pristine system. $H_{15}C_{30}B$ + Co has the highest adsorption energy (−1.86 eV) among all other B/N/S-doped CQDs. Interestingly, rectangular $H_{15}C_{30}N$ + Co has an adsorption energy (−1.04 eV) larger than that of $H_{15}C_{31}$ + Co (0.39 eV). A similar observation was made by Jin *et al.*, for the adsorption of Co on graphenes.[94] The adsorption energy (−0.27 to −0.31 eV) and interaction

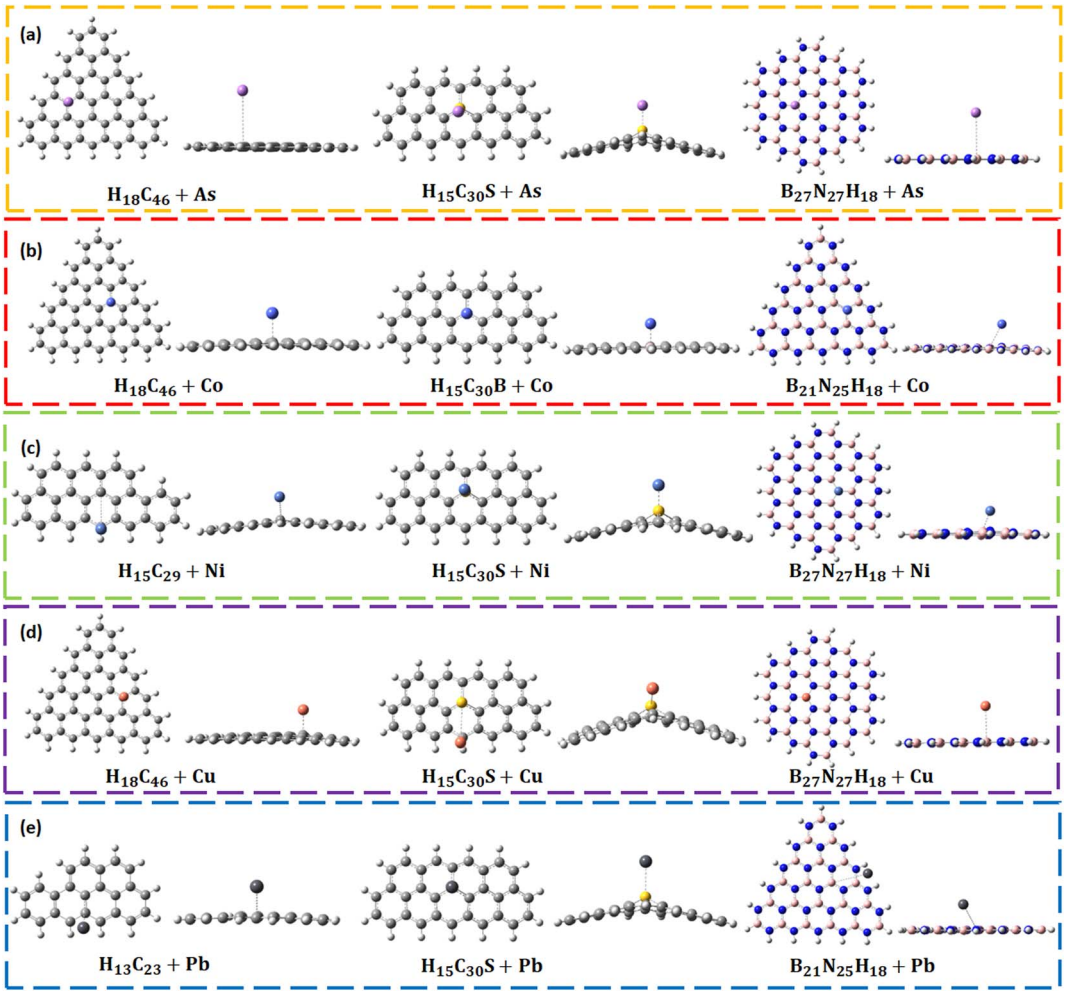

Fig. 3 Optimized structures of QD + metals: (a) As, (b) Co, (c) Ni, (d) Cu, and (e) Pb complexes having higher adsorption energies.

distance (2.34 to 2.83 Å) of BNQDs on Co interaction suggest that Co is physisorbed on these BNQDs with different morphologies and the adsorption energy range is modest. The planarity gets reduced on Co interaction and the highest change occurs for $N_{16}B_{15}H_{15}$ + Co.

3.4.3 Nickel. After the adsorption of Ni in pristine CQDs, there is no appreciable change in the C–C–C bond angles and planarity. The calculated adsorption energies (−1.63 to −2.56 eV) and interaction distance values (1.96 to 3.96 Å) of Ni on CQDs suggest that mostly Ni is chemisorbed over it and rectangular $H_{15}C_{29}$ + Ni has the highest adsorption energy (−2.56 eV). In systems with circular morphology, $H_{18}C_{54}$ + Ni has the lowest adsorption energy (−1.63 eV), which means it is chemisorbed too. The lowest adsorption energy on circular CQDs can be attributed to their high stability, as it has a large energy gap. The chemisorption is attributed to the strong hybridization between the d orbitals of Ni and the π (p_z) orbitals of CQD. These observations are in line with the findings of Gong *et al.*[95]

After the interaction of Ni with B/N/S-doped rectangular CQDs, there is no appreciable change in the C–C–C bond angles and C-(B/N)–C bond angle, except C–S–C. The C–S–C bond angle has changed by 19.84°. The planarity gets disturbed on this interaction, and the planarity of rectangular $H_{15}C_{30}S$ + Ni (35.62°) gets affected more. The adsorption energy of Ni on these systems (−1.38 to −4.22 eV) suggests that it gets chemisorbed. Ni metal shows good bond formation with S of $H_{15}C_{30}S$ during interaction, an interaction distance of 2.00 Å matches the bond length of the NiS system.[96] $H_{15}C_{30}S$ + Ni has the highest adsorption energy (−4.21 eV) among all other QDs. The interaction between Ni and B/N doped CQD is due to the hybridization between 3 d orbitals of Ni and 2p orbitals of B/N atoms of CQD, a similar observation was made by Zhou *et al.*, for B/N-doped graphenes.[97]

The adsorption energy values (−1.44 to −1.47 eV) are nearly the same for all BNQDs with Ni and the interaction distance (2.42 to 2.45 Å) between BNQDs and Ni suggests the chemisorption between the two entities. A negligible change in the diameter is observed in Ni interaction with BNQDs because of very little distortion and stability of BNQDs. The interaction of Ni with circular BNQDs ($N_{27}B_{27}H_{18}$) is the highest (−1.47 eV).

3.4.4 Copper. In Cu-adsorbed pristine CQDs, there is no appreciable change occurring to the C–C–C bond angles and planarity, except triangular CQDs ($H_{18}C_{46}$ + Cu). The adsorption energies (−1.01 to −1.06 eV) and interaction distance values

(3.50 to 3.79 Å) of Cu on CQDs suggest that mostly Cu is chemisorbed over it. Triangular $H_{18}C_{46}$ + Cu has the highest adsorption energy (−1.56 eV) compared to all CQDs. The high interaction of copper with CQDs is due to the strong hybridization between the 3d orbitals of Cu and the p orbitals of CQDs. A similar observation was made by Nakada *et al.*, for graphenes.[98]

The adsorption energies of Cu on B/N/S-doped rectangular CQDs are from −0.84 to −3.72 eV. The adsorption energy (−0.84 eV) and interaction distance of 3.92 Å were observed when Cu interacts with $H_{15}C_{30}N$, which suggests that Cu is physisorbed. Cu interaction with $H_{15}C_{30}S$ and $H_{15}C_{30}B$ shows chemisorption with adsorption energies of −3.72 eV and −1.44 eV, respectively with the former having the highest adsorption energy. Due to the strong interaction, the C–S–C bond angle has changed by 19.10°. The planarity gets disturbed more with an out-of-plane projection of about 42.50° in $H_{15}C_{30}S$ + Cu. Similarly, the diameter of $H_{15}C_{30}S$ + Cu varied (0.61 Å) much from its pristine system. For systems $H_{15}C_{30}S$ + Cu and $H_{15}C_{30}N$ + Cu, the diameter gets reduced on Cu interaction. The chemical bonding between Cu and B/N-doped CQD is due to the interaction between the 2p orbitals of C and B/N and the d orbitals of the Cu atom. A similar observation was made by An and Turner on the interaction study of Cu with B/N-doped single-walled carbon nanotubes.[99]

The adsorption energies (−0.23 to −0.25 eV) and interaction distance (3.22 to 3.35 Å) of BNQDs + Cu complexes suggest that Cu is physisorbed on these BNQDs. It suggests weak interaction between Cu and BNQDs and our observations are in line with Liu *et al.*[100] The N–B–N and B–N–B bond angles have changed by 0.83° and 0.38°, respectively in $B_{15}N_{16}H_{15}$ + Cu. The planarity gets reduced on Cu interaction and the highest change occurs for $B_{15}N_{16}H_{15}$ + Cu by about 1.26°.

3.4.5 Lead. The adsorption energies (−0.18 to −2.08 eV) and interaction distance values (2.42 to 4.07 Å) of Pb on CQDs suggest that mostly Pb is chemisorbed over it. Rectangular $H_{13}C_{23}$ + Pb has the highest adsorption energy (−2.08 eV). Our observations are in line with the findings of Shtepliuk *et al.*[76] The higher interaction of Pb with pristine CQDs is due to the presence of 2 unpaired electrons in the 6p orbital of Pb.[101] Strong hybridization between the HOMO and LUMO of both Pb and CQD leads to a decrease in the energy gap. A similar kind of observation was reported by Shtepliuk *et al.*, for the interaction of Pb with graphene QDs.[76]

The adsorption energies of Pb on B/N/S-doped CQDs (−0.79 to −3.32 eV) suggest that it gets chemisorbed. An adsorption energy of −0.79 eV and an interaction distance of 3.88 Å were observed when Pb interacted with $H_{15}C_{30}N$. A similar observation was made by Srivastava *et al.*, for Pb with B and N-doped graphenes, which has occurred due to the nucleophilic behaviour of the N-doped CQD.[102] $H_{15}C_{30}S$ + Pb has the highest adsorption energy (−3.32 eV) among all other QDs. The C–S–C bond angle changed by 18.69°. The planarity gets disturbed on this interaction, and the planarity of $H_{15}C_{30}S$ + Pb (35.62°) gets affected more. The Pb metal shows good bond formation with S of $H_{15}C_{30}S$ during the interaction. The interaction distance of 2.85 Å matches the bond length of the Galena (PbS) system.[103]

The adsorption energies (−0.15 to −0.47 eV) and interaction distance (3.26 to 4.71 Å) of Pb-adsorbed BNQDs suggest that Pb is physisorbed on the latter. The interaction of Pb with circular BNQDs ($B_{27}N_{27}H_{18}$) is the lowest. This may be due to the high stability of circular BNQDs.

In summary, pristine rectangular $H_{15}C_{31}$ and circular $H_{18}C_{54}$ CQDs showed the highest adsorption towards Ni. Meanwhile, triangular $H_{18}C_{46}$ CQDs showed the highest adsorption towards As. Both B/N-doped CQDs showed more affinity toward Pb. Furthermore, S-doped CQDs showed the highest interaction with Cu. Interestingly, BNQDs of all morphologies showed the highest interaction with As. More importantly, pristine triangular and S-doped CQDs showed a larger affinity towards all toxic metals. We propose the following facts based on the nature of interaction and the magnitude of the obtained adsorption energies of metals with the considered QDs. Most of the metals interact with the pristine and B/N/S-doped CQDs with higher adsorption energies ensuring chemisorption. Such QDs can also be used as adsorbents or filters in the process of obtaining clean drinking water.[101,104] Furthermore, the BNQDs have shown physisorption towards all toxic metals enabling them to be reused. Hence, BNQDs can be more efficient optical sensors than CQDs.

3.5 Interaction studies of toxic metals with QDs in water phase

PCM was employed to include the effect of solvent, *i.e.* water. The PCM uses continuous solvent distribution to describe the interaction between the solute and the solvent. In this section, the changes in the adsorption energy, formation energy and dipole moment after metal complexation with QDs in the water phase were analyzed. The calculated formation energies of QD + metal complexes are negative, confirming their complexation stability in the water phase (Table S1†). We can observe a large change in the dipole moments in all QDs after the interaction with toxic metals (Table S2†). An increase in the dipole moment of the complex was observed due to a change in the charge distribution due to the effect of water.[105]

3.5.1 Arsenic. A large change in dipole moment occurs for rectangular $H_{15}C_{29}$ + As of about 3.64 debye. The lowest change in dipole moment is noted for circular $H_{18}C_{46}$ + As. In the water phase, the highest adsorption energy was observed for triangular $H_{18}C_{46}$ + As (−3.10 eV). A similar trend was observed in the adsorption energy of triangular $H_{18}C_{46}$ + As in the gas phase. In B/N/S-doped CQDs, the highest adsorption energy was observed for $H_{15}C_{30}S$ + As (−3.14 eV) similar to the gas phase. There was a large change in dipole moment of about 8.88 debye in $H_{15}C_{30}S$ + As. Similar to pristine and B/N/S-doped CQDs, the interaction of As with BNQDs leads to an increase in the dipole moment. A large change in dipole moment occurs for rectangular $B_{15}N_{16}H_{15}$ + As by about 2.58 debye. The lowest change in dipole moment under the influence of water occurs for triangular $B_{21}N_{25}H_{18}$ + As (0.11 debye). The highest adsorption energy is observed for $B_{15}N_{16}H_{15}$ + As (−0.91 eV). Less change in dipole moment was observed for $B_{27}N_{27}H_{18}$ + As, and this could be due to the uniform distribution of charges over the structure and

symmetric shape of circular BNQDs ($N_{27}B_{27}H_{18}$), as reported by Miah *et al.*, for BN nanostructures.[106]

3.5.2 Cobalt. A large change in dipole moment of about 12.04 debye occurs for triangular $H_{18}C_{46}$ + Co. The lowest change in dipole moment is observed in circular $H_{13}C_{25}$ + Co. In the water phase, the highest adsorption energy was observed for triangular $H_{18}C_{46}$ + Co (−2.65 eV). A similar trend was observed in the adsorption energy of triangular $H_{18}C_{46}$ + Co in the gas phase. Rectangular $H_{15}C_{31}$ + Co has a positive adsorption energy, which implies that Co interaction with $H_{15}C_{31}$ is unfavourable in the water phase. In B/N/S-doped CQDs, a large change in dipole moment of about 8.22 debye occurs for $H_{15}C_{30}N$ + Co. The lowest change in dipole moment is evidenced in $H_{15}C_{30}B$ + Co. In the water phase, the highest adsorption energy was observed for rectangular $H_{15}C_{30}B$ + Co (−2.44 eV), and a similar trend was observed for adsorption energy for $H_{15}C_{30}B$ + Co in the gas phase. A large change in dipole moment of about 1.78 debye occurs for rectangular $B_{15}N_{16}H_{15}$ + Co. The lowest change in dipole moment is recorded for circular $B_{21}N_{25}H_{18}$ + Co. Less change in dipole moment was observed for $B_{27}N_{27}H_{18}$ + Co. This could be due to the uniform distribution of charges over the structure and the symmetric shape of circular BNQDs ($B_{27}N_{27}H_{18}$). The highest adsorption energy is observed in $N_{25}B_{21}H_{18}$ + Co (−0.27 eV), and the same trend is observed in gas phase too.

3.5.3 Nickel. A large change in dipole moment of about 19.07 debye occurs for triangular $H_{18}C_{46}$ + Ni. The lowest change in dipole moment is noted for circular $H_{18}C_{54}$ + Ni. This could be due to the symmetric shape and charge distribution in circular CQDs, which agrees with the similar observation made by Miah *et al.*, for graphene nanosheets.[106] In the water phase, the highest adsorption energy was observed for triangular $H_{18}C_{46}$ + Ni (−3.29 eV), whereas in the gas phase, the highest adsorption energy was observed for rectangular $H_{15}C_{29}$ + Ni. Ni interaction with B/N/S-doped CQDs under the influence of water leads to an increase in the dipole moment. A large change in dipole moment of about 14.64 debye occurs for $H_{15}C_{30}S$ + Ni. This confirms a stronger interaction between Ni and $H_{15}C_{30}S$. The lowest change in dipole moment is observed in $H_{15}C_{30}N$ + Ni. Similar to pristine and B/N/S-doped CQDs, the interaction of Ni with BNQDs leads to an increase in the dipole moment. A large change in dipole moment of about 2.50 debye occurs for rectangular $B_{15}N_{16}H_{15}$ + Ni. The lowest change in dipole moment is noted in circular $B_{27}N_{27}H_{18}$ + Ni. The highest adsorption energy is obtained in $B_{27}N_{27}H_{18}$ + Ni (−1.52 eV) similar to the gas phase results.

3.5.4 Copper. A large change in dipole moment of about 6.35 debye occurs for triangular $H_{18}C_{46}$ + Cu. The lowest change in dipole moment under the influence of water occurs for circular $H_{18}C_{54}$ + Cu, which could be due to the symmetric shape and charge distribution in circular CQDs. In the water phase, the highest solvation energy was observed for triangular $H_{18}C_{46}$ + Cu (−1.79 eV), and a similar trend was observed in the adsorption energy of triangular $H_{18}C_{46}$ + Cu in the gas phase also. A large change in dipole moment occurs for $H_{15}C_{30}S$ + Cu by about 3.74 debye. The lowest change in dipole moment under the influence of water occurs for $H_{15}C_{30}N$ + Cu. In the water phase, the highest solvation energy was observed for rectangular $H_{15}C_{30}S$ + Cu (−3.90 eV). A large change in dipole moment of about 1.96 debye occurs for rectangular $B_{15}N_{16}H_{15}$ + Cu. The lowest change in dipole moment under the influence of water occurs for circular $B_{27}N_{27}H_{18}$ + Cu. Here too, the highest adsorption energy is obtained in $B_{27}N_{27}H_{18}$ + Cu (−0.25 eV) similar to the gas phase results.

3.5.5 Lead. A large change in dipole moment of about 10.17 debye occurs for rectangular $H_{15}C_{31}$ + Pb. The increase in the dipole moment leads to an increase in the interaction of CQDs with Pb, and a similar observation was made by Abdelsalam *et al.*, for the interaction study of Pb with graphene QDs.[107] The lowest change in dipole moment under the influence of water occurs for circular $H_{18}C_{54}$ + Pb. In the water phase, the highest solvation energy was observed for triangular $H_{18}C_{46}$ + Pb (−2.10 eV), whereas the highest adsorption energy in the gas phase was observed for the same. A large change in dipole moment occurs for $H_{15}C_{30}N$ + Pb by about 5.92 debye. The lowest change in dipole moment under the influence of water occurs for $H_{15}C_{30}S$ + Pb. In the water phase, the highest solvation energy was observed for rectangular $H_{15}C_{30}S$ + Pb (−3.04 eV), and a similar trend was observed for adsorption energy for B/N/S-doped CQDs with Pb. A large change in dipole moment of about 2.10 debye occurs for rectangular $B_{15}N_{16}H_{15}$ + Pb. The lowest change in dipole moment under the influence of water occurs for circular $B_{27}N_{27}H_{18}$ + Pb. The highest solvation energy is observed for $B_{21}N_{25}H_{18}$ + Pb (−0.25 eV), which agrees with the trend observed for the adsorption energy of BNQDs with Pb in the gas phase.

3.6 Detection of toxic metals using UV-vis absorption spectra in the water phase

The UV-vis absorption spectra of QDs with metals (As, Co, Ni, Cu, Ni, and Pb) in the water phase were recorded (Fig. 4). After the interaction of metals with QDs, there is either a decrease or an increase in the absorbance peaks when compared to the absorption spectra of bare QDs (Table 2). This percentage of change is quantified based on the intensity variation of the absorption peaks before and after interaction with metals.

3.6.1 Pristine CQDs. The decrement in the absorption peak intensity was observed for rectangular CQDs ($H_{15}C_{31}$) with metals (Pb, Ni, and Co). Similarly, fluorescence quenching has been reported on the adsorption of Co and Pb in the CQDs and carbon dots by Kong *et al.*, and Sun *et al.*, respectively.[108,109] A similar observation was made by Noun *et al.* and Liu *et al.* during the detection of Pb^{2+} ions using carbon dots.[110,111] The percentage of decrement of absorbance for metals with rectangular $H_{15}C_{31}$ CQDs ranges from 13.19 to 61.31%. The highest percentage of decrement of absorbance was observed for Pb with $H_{15}C_{31}$ (61.31%). Moreover, it was observed that the peak intensity increased by about 3.56% after Cu adsorption with $H_{15}C_{31}$. In addition, the interaction of rectangular $H_{15}C_{31}$ with metals mostly results in peak shift. The maximum absorption peak has shifted from 259 to 433 nm, resulting in a red shift in Cu, Co, Ni and Pb. Strikingly, the rectangular $H_{15}C_{31}$ CQD shows a blue shift with As. The redshift can be due to the

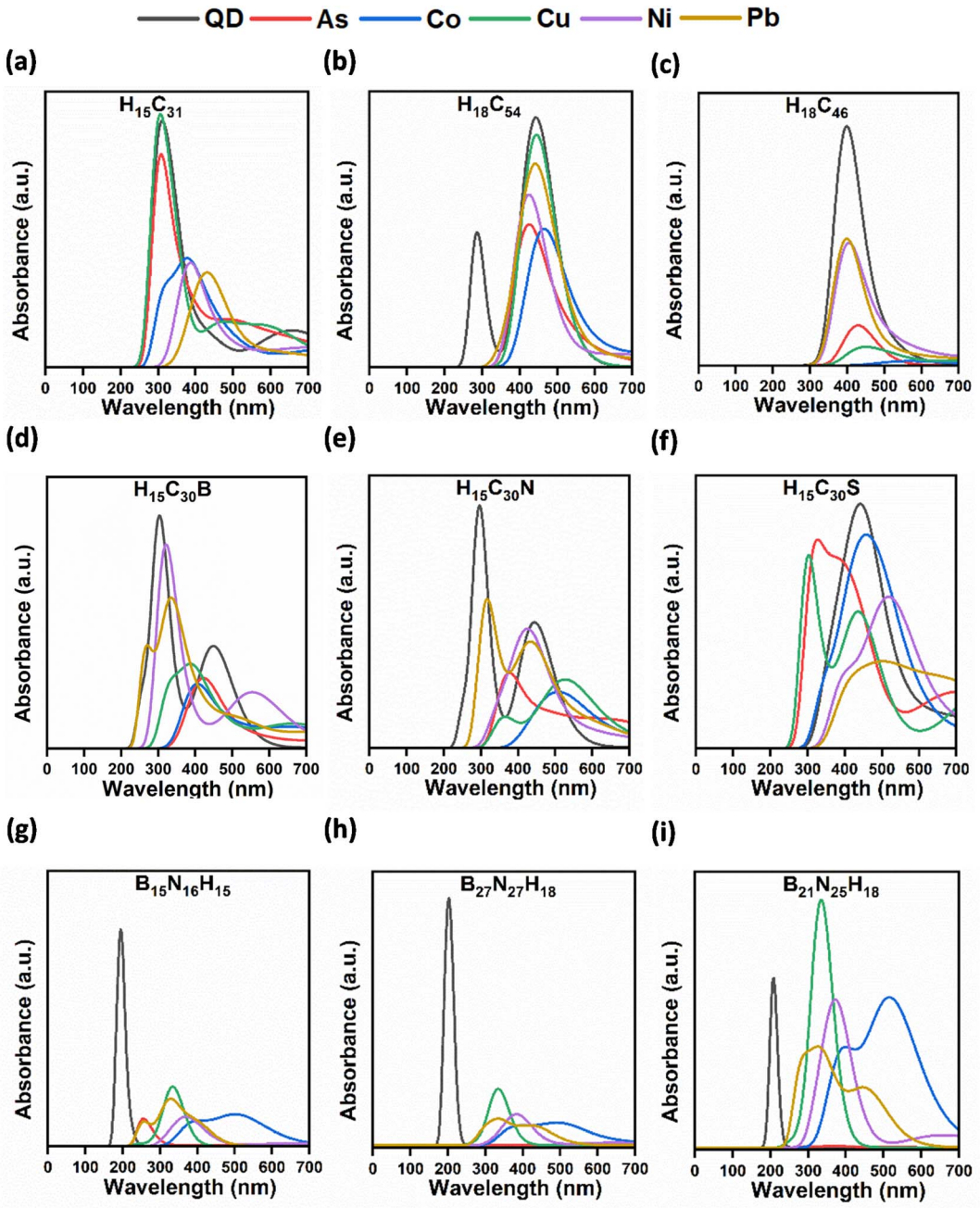

Fig. 4 UV-vis absorption spectra of QDs: (a) rectangular CQDs ($H_{15}C_{31}$), (b) circular CQDs ($H_{18}C_{54}$), (c) triangular CQDs ($H_{18}C_{46}$), (d) rectangular boron-doped CQDs ($H_{15}C_{30}B$), (e) rectangular nitrogen-doped CQDs ($H_{15}C_{30}N$), (f) rectangular sulphur-doped CQDs ($H_{15}C_{30}S$), (g) rectangular BNQDs ($B_{15}N_{16}H_{15}$), (h) circular BNQDs ($B_{27}N_{27}H_{18}$), and (i) triangular BNQDs ($B_{21}N_{25}H_{18}$) with metals (As, Co, Cu, Ni, and Pb).

decrease in the energy gap of rectangular CQDs after interaction with metals.[112] The percentage of reduction for metals with circular $H_{18}C_{54}$ CQDs ranges from 6.88 to 44.61%. A maximum intensity reduction (44.61%) was observed after Co interaction. Moreover, the interaction with metals (Pb, Co, and Cu) has led to a redshift from 443 to 463 nm. The adsorption of As led to a blue shift, with a peak shift from 443 to 423 nm.

Upon interaction of metals with triangular $H_{18}C_{46}$ CQDs, the absorption peak intensity reduction was observed. A maximum decrease in the absorbance was observed for triangular $H_{18}C_{46}$ + Co. The percentage of absorption reduction for metals with triangular CQDs ranges from 46.96 to 98.17%. The highest percentage of intensity diminution was observed for Co with $H_{18}C_{46}$ (98.17%). The interaction of triangular CQDs with metals results in a redshift with the absorption peaks shifting from 400 to 573 nm. Our findings on the absorption reduction of Cu, Co, and Pb using circular and triangular CQDs are in line with the previously reported observations on quenching and decrease in the intensity of emission/fluorescence spectra upon the addition of metals to CQDs in water.[113–115]

Table 2 Percentage of peak intensity modulation after metal complexation with QDs

	Calculated percentage of absorbance reduction/increment (%)				
Morphology/QD	As	Co	Ni	Cu	Pb
Rectangular $H_{15}C_{31}$	13.19	55.42	57.48	3.56[a]	61.31
Circular $H_{18}C_{54}$	42.81	44.61	30.88	6.88	18.60
Triangular $H_{18}C_{46}$	83.20	98.17	47.89	92.22	46.96
Rectangular $H_{15}C_{30}B$	69.57	72.29	12.20	63.98	34.95
Rectangular $H_{15}C_{30}N$	68.16	77.11	50.11	71.33	38.04
Rectangular $H_{15}C_{30}S$	14.66	12.58	38.02	21.24	63.64
Rectangular $B_{15}N_{16}H_{15}$	87.72	85.34	86.45	72.85	78.10
Circular $B_{27}N_{27}H_{18}$	99.96	90.90	87.54	77.30	89.31
Triangular $B_{21}N_{25}H_{18}$	99.16	11.32	12.89	44.94[a]	40.41

[a] % increment in the absorbance peak intensity.

3.6.2 B/N/S-doped CQDs. The percentage of absorption decline for metals with rectangular B-doped CQDs ranges from 12.20 to 72.29%. The highest percentage of intensity reduction was observed for Co with $H_{15}C_{30}B$ (72.29%). This reduction occurs due to charge and energy transfer between metal and rectangular boron-doped CQDs ($H_{15}C_{30}B$).[116] Our findings of absorbance reduction in Pb and Cu-adsorbed rectangular B-doped CQD matches with the observations made by Wang *et al.*, for the detection of Pb^{2+} and Cu^{2+} ions using B-doped carbon dots from fluorescence emission spectra.[116] The interaction of rectangular B-doped CQDs with metals results in a redshift with the peaks shifting from 303 to 426 nm.

The percentage of absorbance reduction for metals with rectangular N-doped CQDs ranges from 38.04 to 77.11%. The highest percentage of quenching is observed for Co with $H_{15}C_{30}N$ (77.11%). The quenching of metals (Cu, Pb, and Co) such as using N-doped CQDs in line with previously reported observations based on photoluminescence emission and fluorescence spectra.[117–119] This decrement has occurred due to charge and energy transfer between metal and rectangular N-doped CQDs. Fluorescence quenching was observed by Wu *et al.* during the detection of Cu^{2+} ions using N-doped CQDs.[120] The interaction of rectangular N-doped CQDs with metals resulted in a redshift of peaks from 299 to 530 nm.

The percentage of absorbance abatement for metals with rectangular S-doped CQDs ranges from 12.58 to 63.64%. The highest percentage of quenching is achieved for Pb with $H_{15}C_{30}S$ (63.64%). A significant amount of reduction agrees well with the interaction energy of rectangular S-doped CQDs with Pb, as it shows a higher interaction energy. The decrement occurs due to charge and energy transfer between metal and rectangular S-doped CQDs, due to the higher binding affinity of S towards metals.[121] The absorbance peak reduction in Pb-adsorbed S-doped CQDs matches with the observations of Bian *et al.* on the detection of Pb^{2+} ions using S-doped graphene QDs in fluorescence spectra.[121] The interaction of metals with rectangular S-doped CQD resulted in a redshift of the peaks from 305 to 510 nm.

3.6.3 BNQDs. The percentage of absorption reduction for metals with rectangular BNQDs ranges from 72.85 to 87.72%. The highest percentage of reduction was observed for As with $B_{15}N_{16}H_{15}$ (87.72%). Our observations of peak intensity reduction in Ni, Cu, and Pb using rectangular, circular, and triangular BNQDs are in line with the observations made by Yao *et al.*, and Liu *et al.*, for the detection of Ni^{2+}, Cu^{2+}, and Pb^{2+} using BNQDs based on fluorescence and photoluminescence spectra.[36,37] The interaction of rectangular BNQDs with metals leads to a redshift with the absorption peaks shifting from 193 to 506 nm. A similar trend as above is observed during the interaction of metals with circular BNQDs ($B_{27}N_{27}H_{18}$). The percentage of reduction for metals with circular BNQDs ranges from 77.30 to 99.96%. The highest percentage is observed for As with $B_{27}N_{27}H_{18}$ (99.96%). The interaction of circular BNQDs with metals leads to a red shift with the absorption peaks shifting from 201 to 497 nm. The percentage of peak intensity decrement after metal complexation with triangular BNQDs ($B_{21}N_{25}H_{18}$) ranges from 11.32 to 99.16% except for Cu. The interaction of Cu has resulted in a peak intensity increment of about 44.94%. The highest percentage of intensity reduction was observed for As with $B_{21}N_{25}H_{18}$ (99.16%). Interestingly, the interaction of triangular BNQD with metals leads to a red shift in the UV-vis absorption spectrum with the absorption peaks shifting from 209 to 515 nm. The redshift in the UV-vis absorption spectra in all BNQD + metal complexes may be due to the decrease in the energy gap of the BNQDs upon interaction with the metals. Overall, the above-mentioned

Table 3 Comparison of the lifetime of QDs with metals

	Lifetime (ns)										
	Calculated lifetime					Experimentally observed lifetime					
Morphology/QD	As	Co	Ni	Cu	Pb	As	Co	Ni	Cu	Pb	References
Rectangular $H_{15}C_{31}$	0.79	5.54	2.16	0.60	4.77	—	—	—	5.40	3.35 to 3.58	109 and 127
Circular $H_{18}C_{54}$	1.76	2.79	2.79	1.14	1.65	—	—	—	5.40	3.35 to 3.58	109 and 127
Triangular $H_{18}C_{46}$	4.63	152.30	1.63	20.14	1.29	—	—	—	5.40	3.35 to 3.58	109 and 127
Rectangular $H_{15}C_{30}B$	3.85	4.86	1.50	2.31	1.94	—	—	—	1.92 to 5.11	1.92 to 4.80	116
Rectangular $H_{15}C_{30}N$	2.14	6.77	2.82	4.76	0.81	—	—	—	5.54	—	128
Rectangular $H_{15}C_{30}S$	1.39	6.73	4.16	1.76	21.29	—	—	—	—	—	—
Rectangular $B_{15}N_{16}H_{15}$	4.55	17.53	9.94	2.86	6.67	—	—	Very small	—	—	36
Circular $B_{27}N_{27}H_{18}$	2992.39	19.99	8.84	3.03	15.35	—	—	Very small	—	—	36
Triangular $B_{21}N_{25}H_{18}$	1198.77	14.69	9.73	3.23	10.87	—	—	Very small	—	—	36

observations of UV-vis absorption peak intensity modulation, and peak shifts demonstrate that these QDs can be used as optical probes for the detection of the toxic metals in drinking water.

3.7 Lifetime of QDs in water phase

Lifetime is one of the important characteristics of QDs. This depends on many internal factors such as the structure of fluorophore (QDs), and also external factors such as temperature, polarity, and the presence of quenchers (metals). When the timescale is in several nanoseconds, it is called fluorescence.[122] Here, we calculated the lifetime of all QDs before and after metal adsorption in the water phase. The obtained lifetime range suggests fluorescence in all QDs. Moreover, we can observe that the lifetime values change concerning the size and morphology of the QDs.

3.7.1 Pristine CQDs. Rectangular CQDs ($H_{15}C_{31}$) have the lowest lifetime of 0.43 ns. The lifetime of circular CQDs ($C_{54}H_{18}$) and triangular CQDs ($C_{46}H_{18}$) is 1.04 ns and 0.56 ns, respectively. These values are in line with the reports of Röding *et al.*, on graphene QDs. A variation in lifetime was observed depending on the size of the CQD.[123]

3.7.2 B/N/S-doped CQDs. The highest lifetime is obtained for $H_{15}C_{30}S$ (2.38 ns). $H_{15}C_{30}N$ (0.29 ns) and $H_{15}C_{30}B$ (0.36 ns) have less lifetime. The order of lifetime and fluorescence observed in B/N/S-doped CQDs is in line with the previously reported observations.[124–126] Interestingly, the lifetime value is higher in $H_{15}C_{30}S$ than in its pristine counterpart $H_{15}C_{31}$. The opposite is observed in $H_{15}C_{30}N$ and $H_{15}C_{30}B$.

3.7.3 BNQDs. Triangular $B_{21}N_{25}H_{18}$ has the highest lifetime (2.02 ns). The lowest lifetime of about 0.40 ns is obtained for rectangular BNQDs ($B_{15}N_{16}H_{15}$). The lifetime of circular BNQD ($B_{27}N_{27}H_{18}$) is 0.69 ns. The order of lifetime and fluorescence observed in BNQDs is in line with the previously reported observations.[28]

3.8 Lifetime of QDs with toxic metals in water phase

3.8.1 CQDs. The lifetime range (0.79 to 4.77 ns) of rectangular $H_{15}C_{31}$ CQD with metals (Pb, Co, Cu, Ni, and As) suggests fluorescence in those systems. Similarly, fluorescence has been observed in circular CQDs ($H_{18}C_{54}$) and triangular CQDs ($H_{18}C_{46}$) after complexation with metals. A similar observation was reported by Sun *et al.*, and Wang *et al.*, during the detection of Pb^{2+} and Cu^{2+} ions using carbon dots respectively.[109,127] Among pristine CQDs, the highest lifetime was observed for triangular $H_{18}C_{46}$ + Co (152.30 ns). The lowest lifetime was observed for rectangular $H_{15}C_{31}$ + As (0.79 ns).

3.8.2 B/N/S-doped CQDs. B/N/S-doped rectangular CQDs exhibit fluorescence after metal adsorption (0.81 ns to 21.29 ns). The highest lifetime has been observed for rectangular $H_{15}C_{30}S$ + Pb (21.29 ns). The lowest lifetime is observed for rectangular $H_{15}C_{30}N$ + Pb (0.81 ns). The magnitude and order of lifetime for Pb and Cu with rectangular $H_{15}C_{30}B$ and Cu with rectangular $H_{15}C_{30}N$ are in close agreement with the observations made by Wang *et al.*, and Zhao *et al.*, towards the detection of Pb^{2+} and Cu^{2+} ions using B-doped and N-doped CQDs, respectively.[116,128]

3.8.3 BNQDs. BNQDs with metals showed fluorescence (2.86 ns to 2.99 μs). The highest lifetime was observed for circular $B_{27}N_{27}H_{18}$ + As (2.99 μs). The lowest lifetime was observed for rectangular $B_{15}N_{16}H_{15}$ + Cu (2.86 ns). The lifetime of a complex of BNQDs with Ni is very short as it is in the order of nanoseconds. This is in agreement with the previous observations reported by Yao *et al.*, during the detection of Ni^{2+} ions using BNQDs.[36] A comparison table between the calculated and experimentally reported lifetimes of QDs with the toxic metals is given in Table 3. The analysis and knowledge on fluorescence lifetime reported here for QDs with metals will help the experimentalists improve the accuracy of metal detection in water.

4. Conclusion

We have investigated the toxic metal (As, Co, Ni, Cu, and Pb) detection capability of QDs (CQDs, B/N/S-doped CQDs, and BNQDs) of various sizes and morphologies (rectangular, circular, and triangular) as potential optical receptors using quantum chemical DFT calculations. Structurally, the circular QDs are very stable. Energy gap analysis has revealed that BNQDs are more stable than CQDs. All toxic metals in the gas phase and water phase get adsorbed in the energy range of −0.02 to −4.21 eV and −0.008 to −4.81 eV, respectively. Among all QDs, pristine triangular CQDs and S-doped CQDs exhibit higher adsorption affinity towards the toxic metals. Most of the QDs show higher interaction with Ni followed by Pb, As, Cu and Co. Moreover, most of the metals are chemisorbed in CQDs and B/N/S-doped CQDs, suggesting such systems to be used as adsorbents. Interestingly, the majority of BNQDs have exhibited physisorption towards the toxic metals. The UV-vis absorption spectra of all QDs indicate the redshift of the absorbance peaks with the increase in the size of the QDs. Raman spectra have confirmed the structural integrity of the modelled QDs. The detection of metals using QDs in the water phase has been understood through absorption peak intensity modulation as observed in the UV-vis absorption spectra. It is noted that BNQDs show the highest percentage of intensity reduction in the UV-vis absorption spectra compared to other QDs after metal adsorption. Reasonably, considerable fluorescence lifetime is obtained for Co with triangular $H_{18}C_{46}$ (152.30 ns) in CQDs, Pb with rectangular $H_{15}C_{30}S$ (21.29 ns) in B/N/S-doped CQDs, and As with circular $B_{27}N_{27}H_{18}$ (2.99 μs) in BNQDs. The nature of interaction of toxic metals as well as the highest degree of absorption peak intensity changes in BNQDs suggests that they can be more efficient than CQDs in the optical sensing of toxic metals. In summary, our extensive DFT studies have demonstrated QDs as optical sensor receptors and the findings will help the experimentalists in designing such environment-friendly probes for the detection of toxic metals in drinking water.

Author contributions

The manuscript was written through the contributions of all authors. All authors have given approval to the final version of the manuscript.

Conflicts of interest

The authors declare no competing financial interest.

Acknowledgements

The authors would like to express their sincere thanks to the crew of the Center for Computational Materials Science of the Institute for Materials Research, Tohoku University, for their continuous support towards supercomputing facilities. Also, the authors thank SRM-HPCC for availing the supercomputer for computations. The authors Y. S. and V. J. S. acknowledge the financial support from DST-SERB under the Core Research Grant (CRG/2021/006647). C. B. S. thanks SRMIST for the fellowship to carry out the research.

References

1 M. Salehi, *Environ. Int.*, 2022, **158**, 106936.
2 Y. Zhang, J. Deng, B. Qin, G. Zhu, Y. Zhang, E. Jeppesen and Y. Tong, *Fundam. Res.*, 2023, **3**, 265–273.
3 R. Kumar, M. Qureshi, D. Kumar and N. Al-ansari, *Case Stud. Chem. Environ. Eng.*, 2022, **6**, 100219.
4 N. A. A. Qasem, R. H. Mohammed and D. U. Lawal, *npj Clean Water*, 2021, **4**, 1–15.
5 N. Verma and R. Sharma, *Recent Pat. Biotechnol.*, 2017, **11**, 171–187.
6 S. Fahimirad and M. Hatami, *Med. Plants Environ. Challenges*, 2017, pp. 189–214.
7 A. Lace and J. Cleary, *Chemosensors*, 2021, **9**, 60.
8 H. N. M. Ekramul Mahmud, A. K. Obidul Huq and R. B. Yahya, *RSC Adv.*, 2016, **6**, 14778–14791.
9 M. N. Nadagouda, C. White and D. Lytle, *Microsc. Microanal.*, 2011, **17**, 284–291.
10 L. Leyssens, B. Vinck, C. Van Der Straeten, F. Wuyts and L. Maes, *Toxicology*, 2017, **387**, 43–56.
11 Z. Haftu and P. Sathishkumar, *Chem. Afr.*, 2020, **3**, 419–426.
12 W. E. Omer, M. F. Abdelbar, N. M. El-Kemary, N. Fukata and M. A. El-Kemary, *RSC Adv.*, 2021, **11**, 31047–31057.
13 C. Huang, H. Dong, Y. Su, Y. Wu, R. Narron and Q. Yong, *Nanomaterials*, 2019, **9**, 387.
14 X. Li, K. Vinothini, T. Ramesh and M. Rajan, *Drug Delivery*, 2020, **27**, 791–804.
15 W. Chen, Z. Qin, B. McElhenny, F. Zhang, S. Chen, J. Bao, Z. M. Wang, H.-Z. Song and Z. Ren, *J. Mater. Chem. A*, 2019, **7**, 21488–21495.
16 P. Devi, P. Rajput, A. Thakur and K. Kim, *Trends Anal. Chem.*, 2019, **114**, 171–195.
17 S. Y. Lim, W. Shen and Z. Gao, *Chem. Soc. Rev.*, 2015, **44**, 362–381.
18 T. Vyas and A. Joshi, *Analyst*, 2024, **149**, 1297–1309.
19 F. Wang, Q. Hao, Y. Zhang, Y. Xu and W. Lei, *Microchim. Acta*, 2016, **183**, 273–279.
20 U. Abd Rani, L. Y. Ng, C. Y. Ng and E. Mahmoudi, *Adv. Colloid Interface Sci.*, 2020, **278**, 102124.
21 J. Dhariwal, G. K. Rao and D. Vaya, *RSC Sustainability*, 2024, **2**, 11–36.
22 S. D. T. Landa, N. K. R. Bogireddy, I. Kaur, V. Batra and V. Agarwal, *Iscience*, 2022, **25**, 103816.
23 Q. Yang, J. Duan, W. Yang, X. Li, J. Mo, P. Yang and Q. Tang, *Appl. Surf. Sci.*, 2018, **434**, 1079–1085.
24 Y. Hu, J. Yang, J. Tian, L. Jia and J.-S. Yu, *Carbon*, 2014, **77**, 775–782.
25 P. M. Revabhai, R. K. Singhal, H. Basu and S. K. Kailasa, *J. Nanostruct. Chem.*, 2023, **13**, 1–41.
26 J. Rawat, D. Sajwan, S. V. Garimella, H. Sharma and C. Dwivedi, *NanoTrends*, 2023, **2**, 100008.
27 X. Zhang, L. An, C. Bai, L. Chen and Y. Yu, *Mater. Today Chem.*, 2021, **20**, 100425.
28 Y. Ding, P. He, S. Li, B. Chang, S. Zhang, Z. Wang, J. Chen, J. Yu, S. Wu and H. Zeng, *ACS Nano*, 2021, **15**, 14610–14617.
29 S. Umrao, A. K. Maurya, V. Shukla, A. Grigoriev, R. Ahuja, M. Vinayak, R. R. Srivastava, P. S. Saxena, I. K. Oh and A. Srivastava, *Mater. Today Bio*, 2019, **1**, 100001.
30 W. Guo, Y. Yang, Q. Jin, H. Zhao, R. Zhang and Y. Zhai, *J. Mater. Sci. Mater. Electron.*, 2021, **32**, 9946–9955.
31 L. Chen, X. Zhang, Z. Zhao, F. Wang, Y. Huang, C. Bai, L. An and Y. Yu, *Colloids Surf., A*, 2021, **614**, 126181.
32 X. Wang, L. Kong, S. Zhou, C. Ma, W. Lin, X. Sun, D. Kirsanov, A. Legin, H. Wan and P. Wang, *Talanta*, 2022, **239**, 122903.
33 Z. Wang, B. Yao, Y. Xiao, X. Tian and Y. Wang, *Chemosensors*, 2023, **11**, 405.
34 V. R. Nair, M. Shanthil, K. Sandeep, K. U. Savitha, A. Archana, V. Deepamol, C. Swetha and P. V. Vaishag, *ACS Omega*, 2023, **8**, 29468–29474.
35 L. Gontrani, O. Pulci, M. Carbone, R. Pizzoferrato and P. Prosposito, *Molecules*, 2021, **26**, 5519.
36 Q. Yao, Y. Feng, M. Rong, S. He and X. Chen, *Microchim. Acta*, 2017, **184**, 4217–4223.
37 B. Liu, S. Yan, Z. Song, M. Liu, X. Ji, W. Yang and J. Liu, *Chem. Eur J.*, 2016, **22**, 18899–18907.
38 M. J. Frisch, G. W. Trucks, H. B. Schlegel, G. E. Scuseria, M. A. Robb, J. R. Cheeseman, G. Scalmani, V. Barone, G. A. Petersson, H. Nakatsuji, X. Li, M. Caricato, A. V. Marenich, J. Bloino, B. G. Janesko, R. Gomperts, B. Mennucci, H. P. Hratchian, J. V. Ortiz, A. F. Izmaylov, J. L. Sonnenberg, D. Williams-Young, F. Ding, F. Lipparini, F. Egidi, J. Goings, B. Peng, A. Petrone, T. Henderson, D. Ranasinghe, V. G. Zakrzewski, J. Gao, N. Rega, G. Zheng, W. Liang, M. Hada, M. Ehara, K. Toyota, R. Fukuda, J. Hasegawa, M. Ishida, T. Nakajima, Y. Honda, O. Kitao, H. Nakai, T. Vreven, K. Throssell, J. A. Montgomery, Jr., J. E. Peralta, F. Ogliaro, M. J. Bearpark, J. J. Heyd, E. N. Brothers, K. N. Kudin, V. N. Staroverov, T. A. Keith, R. Kobayashi, J. Normand, K. Raghavachari, A. P. Rendell, J. C. Burant, S. S. Iyengar, J. Tomasi, M. Cossi, J. M. Millam, M. Klene, C. Adamo, R. Cammi, J. W. Ochterski, R. L. Martin, K. Morokuma, O. Farkas, J. B. Foresman, and D. J. Fox, *Gaussian 16, Revision C.01*, Gaussian, Inc., Wallingford CT, 2016.
39 H. Riesen, C. Wiebeler and S. Schumacher, *J. Phys. Chem. A*, 2014, **118**, 5189–5195.

40 M. Javan, R. Jorjani and A. R. Soltani, *J. Mol. Model.*, 2020, **26**, 1–10.
41 R. E. Ambrusi, C. R. Luna, A. Juan and M. E. Pronsato, *RSC Adv.*, 2016, **6**, 83926–83941.
42 K. Li, N. Li, N. Yan, T. Wang, Y. Zhang, Q. Song and H. Li, *Appl. Surf. Sci.*, 2020, **515**, 146028.
43 J. Zhao and J. Ma, *J. Phys. Chem. C*, 2016, **120**, 25131–25141.
44 M. Maruyama and S. Okada, *Sci. Rep.*, 2018, **8**, 16657.
45 S. S. Yamijala, M. Mukhopadhyay and S. K. Pati, *J. Phys. Chem. C*, 2015, **119**, 12079–12087.
46 L. Mishra, R. K. Behera, S. Mondal, S. Kumar, A. Panigrahi and M. K. Sarangi, *Carbon*, 2021, **178**, 594–605.
47 S. S. Yamijala, A. Bandyopadhyay and S. K. Pati, *J. Phys. Chem. C*, 2013, **117**, 23295–23304.
48 B. Sert, S. Gonca, Y. Ozay, E. Harputlu, S. Ozdemir, K. Ocakoglu and N. Dizge, *Colloids Surf., B*, 2021, **205**, 111867.
49 H. R. Jiang, T. S. Zhao, L. Shi, P. Tan and L. An, *J. Phys. Chem. C*, 2016, **120**, 6612–6618.
50 A. El Hadki, K. Ulucan-altuntas, H. El Hadki, C. B. Ustundag, O. K. Kabbaj, A. Dahchour, N. Komiha, A. Zrineh and E. Debik, *FlatChem*, 2021, **27**, 100238.
51 S. Kadian, N. K. Tailor, N. Chaulagain, K. Shankar, S. Satapathi and G. Manik, *J. Mater. Sci. Mater. Electron.*, 2021, **32**, 17406–17417.
52 S. N. Ema, M. A. Khaleque, A. Ghosh, A. A. Piya, U. Habiba and S. U. D. Shamim, *RSC Adv.*, 2021, **11**, 36866–36883.
53 R. Talaei, B. Khalili and M. Mokhtary, *J. Mol. Liq.*, 2020, **304**, 112696.
54 M. M. El-Nahass, M. A. Kamel, A. F. El-Deeb, A. A. Atta and S. Y. Huthaily, *Spectrochim. Acta, Part A*, 2011, **79**, 1499–1504.
55 C.-G. Liu, Z.-M. Su, X.-H. Guan and S. Muhammad, *J. Phys. Chem. C*, 2011, **115**, 23946–23954.
56 M. Ahmed, M. El-Mansy, M. Hassan, M. A. Mostafa, M. A. M. El-Mansy, H. M. Hassanin and M. A. Mostafa, *Org. Optoelectron.*, 2015, **1**, 1.
57 B. Mandal, S. Sarkar and P. Sarkar, *J. Nanopart. Res.*, 2012, **14**, 1–8.
58 N. Kateris, A. S. Jayaraman and H. Wang, *Proc. Combust. Inst.*, 2023, **39**, 1069–1077.
59 M. El Masfioui, S. Bahsine, A. Elbiyaali and F. Allali, in *E3S Web of Conferences*, EDP Sciences, 2022, vol. 336, pp. 48.
60 J. Feng, H. Dong, B. Pang, F. Shao, C. Zhang, L. Yu and L. Dong, *Phys. Chem. Chem. Phys.*, 2018, **20**, 15244–15252.
61 W. Sun, C. Chen, C. Li, D. Wu, J. Kang, Y. Li and Z. Li, *ChemPhysChem*, 2018, **19**, 2518–2524.
62 T. Guerra, L. R. S. Araújo and S. Azevedo, *J. Phys. Chem. Solids*, 2019, **135**, 109085.
63 F. Shayeganfar, M. R. R. Tabar, A. Simchi and J. Beheshtian, *Phys. Rev. B*, 2017, **96**, 165307.
64 G. E. D. Viana, A. M. Silva, F. U. da C. Barros, F. da Silva, E. W. S. Caetano, J. J. S. Melo and A. Macedo-Filho, *J. Mol. Model.*, 2020, **26**, 1–11.
65 F. Zhang, F. Liu, C. Wang, X. Xin, J. Liu, S. Guo and J. Zhang, *ACS Appl. Mater. Interfaces*, 2016, **8**, 2104–2110.
66 M. Zhang, L. Bai, W. Shang, W. Xie, H. Ma, Y. Fu, D. Fang, H. Sun, L. Fan and M. Han, *J. Mater. Chem.*, 2012, **22**, 7461–7467.
67 A. Ananthanarayanan, X. Wang, P. Routh, B. Sana, S. Lim, D. Kim, K. Lim, J. Li and P. Chen, *Adv. Funct. Mater.*, 2014, **24**, 3021–3026.
68 Z. Fan, Y. Li, X. Li, L. Fan, D. Fang and S. Yang, *Carbon*, 2014, **70**, 149–156.
69 Y. Ma, A. Y. Chen, Y. Y. Huang, X. He, X. F. Xie, B. He, J. H. Yang and X. Y. Wang, *Carbon*, 2020, **162**, 234–244.
70 B. Saha and P. K. Bhattacharyya, *ACS Omega*, 2018, **3**, 16753–16768.
71 P. A. Z. Hasibuan, M. Tanjung, W. Lianto, S. Gea, A. Piliang and S. A. Situmorang, *Case Stud. Chem. Environ. Eng.*, 2023, **8**, 100455.
72 F. Wu, M. Yang, H. Zhang, S. Zhu, X. Zhu and K. Wang, *Opt. Mater.*, 2018, **77**, 258–263.
73 S. Sangam, A. Gupta, A. Shakeel, R. Bhattacharya, A. K. Sharma, D. Suhag, S. Chakrabarti, S. K. Garg, S. Chattopadhyay and B. Basu, *Green Chem.*, 2018, **20**, 4245–4259.
74 A. Cuesta, P. Dhamelincourt, J. Laureyns, A. Martinez-Alonso and J. M. D. Tascón, *Carbon*, 1994, **32**, 1523–1532.
75 E. Dervishi, Z. Ji, H. Htoon, M. Sykora and S. K. Doorn, *Nanoscale*, 2019, **11**, 16571–16581.
76 I. Shtepliuk, N. M. Caffrey, T. Iakimov, V. Khranovskyy, I. A. Abrikosov and R. Yakimova, *Sci. Rep.*, 2017, **7**, 3934.
77 N. Venkatesan, K. S. Archana, S. Suresh, R. Aswathy, M. Ulaganthan, P. Periasamy and P. Ragupathy, *ChemElectroChem*, 2019, **6**, 1107–1114.
78 M. P. Kumar, C. Takahashi, S. Kundu, T. N. Narayanan and D. K. Pattanayak, *New J. Chem.*, 2019, **43**, 14313–14319.
79 C. Hsu, L. Laysandra, Y. Chiu and W. Liu, *Chem. Eng. J.*, 2023, **473**, 145469.
80 V. V. Chesnokov, I. P. Prosvirin, E. Y. Gerasimov and A. S. Chichkan, *Materials*, 2023, **16**, 1986.
81 L. Zhang, Z.-Y. Zhang, R.-P. Liang, Y.-H. Li and J.-D. Qiu, *Anal. Chem.*, 2014, **86**, 4423–4430.
82 Y. A. Kim, K. Fujisawa, H. Muramatsu, T. Hayashi, M. Endo, T. Fujimori, K. Kaneko, M. Terrones, J. Behrends and A. Eckmann, *ACS Nano*, 2012, **6**, 6293–6300.
83 R. Atchudan, T. N. J. I. Edison, S. Perumal, N. C. S. Selvam and Y. R. Lee, *J. Photochem. Photobiol., A*, 2019, **372**, 99–107.
84 Y. Liu, L. Jiang, B. Li, X. Fan, W. Wang, P. Liu, S. Xu and X. Luo, *J. Mater. Chem. B*, 2019, **7**, 3053–3058.
85 Z. Zafar and Z. H. Ni, *Carbon*, 2013, **61**, 57–62.
86 M. Ayiania, E. Weiss-Hortala, M. Smith, J.-S. McEwen and M. Garcia-Perez, *Carbon*, 2020, **167**, 559–574.
87 P. Ahmad, M. U. Khandaker, F. Rehman, N. Muhammad, M. R. I. Faruque, Z. Ullah, M. A. R. Khan, G. Khan, M. I. Khan, H. Ali, *et al.*,, *Ceram. Int.*, 2021, **11**, 222.
88 M. Srivastava, A. Srivastava and S. K. Pandey, *Appl. Surf. Sci.*, 2020, 146021.
89 M. Srivastava and A. Srivastava, *Mater. Today: Proc.*, 2022, **48**, 661–665.

90 S. S. Meshkat, S. Hoseinzadeh, Z. Hosseini-dastgerdi, R. Mehrabi, E. Ghasemy and M. Esrafili, *Int. J. Environ. Sci. Technol.*, 2023, **20**, 8287–8302.
91 H. Fuess, T. Kratz, J. Töpel-Schadt and G. Miehe, *Z. Kristallogr. Krist.*, 1987, **179**, 335–346.
92 A. N. Rudenko, F. J. Keil, M. I. Katsnelson and A. I. Lichtenstein, *Phys. Rev. B*, 2012, **86**, 75422.
93 E. L. Uzunova, *Phys. Chem. Chem. Phys.*, 2022, **24**, 20228–20238.
94 C. Jin, L. Cheng, G. Feng, R. Ye, Z.-H. Lu, R. Zhang and X. Yu, *Langmuir*, 2022, **38**, 3694–3710.
95 C. Gong, G. Lee, B. Shan, E. M. Vogel, R. M. Wallace and K. Cho, *J. Appl. Phys.*, 2010, **108**, 123711.
96 K. Sharkas, L. Gagliardi and D. G. Truhlar, *J. Phys. Chem. A*, 2017, **121**, 9392–9400.
97 X. Zhou, W. Chu, W. Sun, Y. Zhou and Y. Xue, *Comput. Theor. Chem.*, 2017, **1120**, 8–16.
98 K. Nakada and A. Ishii, *Graphene Simul.*, 2011, pp. 1–19.
99 W. An and C. H. Turner, *J. Phys. Chem. C*, 2009, **113**, 7069–7078.
100 X. Liu, T. Duan, Y. Sui, C. Meng and Y. Han, *RSC Adv.*, 2014, **4**, 38750–38760.
101 S. M. Elgengehi, S. El-taher, M. A. A. Ibrahim, K. Jacques and K. E. El-kelany, *Appl. Surf. Sci.*, 2019, 145038.
102 M. Srivastava and A. Srivastava, *Mater. Sci. Eng., B*, 2021, **269**, 115165.
103 J. Chen, X. Long and Y. Chen, *J. Phys. Chem. C*, 2014, **118**, 11657–11665.
104 M. K. Hossain, D. Roy and F. Ahmed, *J. Mol. Struct.*, 2021, **1237**, 130302.
105 L. Guo, S. Kaya, I. B. Obot, X. Zheng and Y. Qiang, *J. Colloid Interface Sci.*, 2017, **506**, 478–485.
106 M. H. Miah, M. R. Hossain, M. S. Islam, T. Ferdous and F. Ahmed, *RSC Adv.*, 2021, **11**, 38457–38472.
107 H. Abdelsalam, N. H. Teleb, I. S. Yahia, H. Y. Zahran, H. Elhaes and M. A. Ibrahim, *J. Phys. Chem. Solids*, 2019, **130**, 32–40.
108 D. Kong, F. Yan, Z. Han, J. Xu, X. Guo and L. Chen, *RSC Adv.*, 2016, **6**, 67481–67487.
109 Z. Sun, Y. Zhou, W. Zhou, J. Luo, R. Liu, X. Zhang, L. Zhou and Q. Pang, *Nanoscale*, 2021, **13**, 2472–2480.
110 F. Noun, E. A. Jury and R. Naccache, *Sensors*, 2021, **21**, 1391.
111 Y. Liu, Q. Zhou, J. Li, M. Lei and X. Yan, *Sens. Actuators, B*, 2016, **237**, 597–604.
112 I. Shtepliuk and R. Yakimova, *Materials*, 2018, **11**, 1217.
113 B. Rooj, A. Dutta, S. Islam and U. Mandal, *J. Fluoresc.*, 2018, **28**, 1261–1267.
114 C.-L. Li, C.-C. Huang, A. P. Periasamy, P. Roy, W.-C. Wu, C.-L. Hsu and H.-T. Chang, *RSC Adv.*, 2015, **5**, 2285–2291.
115 T. Ghosh, R. Sahoo, S. K. Ghosh, P. Banerji and N. C. Das, *Front. Chem. Sci. Eng.*, 2023, **17**, 536–547.
116 Z.-X. Wang, X.-H. Yu, F. Li, F.-Y. Kong, W.-X. Lv, D.-H. Fan and W. Wang, *Microchim. Acta*, 2017, **184**, 4775–4783.
117 V. Singh, V. Kumar, U. Yadav, R. Kr and J. ISSS, *Micro Smart Syst.*, 2017, **6**, 109–117.
118 R. Bandi, R. Dadigala and B. Reddy, *J. Photochem. Photobiol., B*, 2018, **178**, 330–338.
119 D. Bano, V. Kumar, S. Chandra, V. K. Singh, S. Mohan, D. K. Singh, M. Talat and S. H. Hasan, *Opt. Mater.*, 2019, **92**, 311–318.
120 X. Wu, L. Wu, X. Cao, Y. Li, A. Liu and S. Liu, *RSC Adv.*, 2018, **8**, 20000–20006.
121 S. Bian, C. Shen, H. Hua, L. Zhou, H. Zhu, F. Xi, J. Liu and X. Dong, *RSC Adv.*, 2016, **6**, 69977–69983.
122 A. Jain, C. Blum and V. Subramaniam, *Advances in Biomedical Engineering*, Elsevier, 2009, pp. 147–176.
123 M. Röding, S. J. Bradley, M. Nydén and T. Nann, *J. Phys. Chem. C*, 2014, **118**, 30282–30290.
124 W. Kwon, J. Lim, J. Lee, T. Park and S.-W. Rhee, *J. Mater. Chem. C*, 2013, **1**, 2002–2008.
125 A. B. Bourlinos, G. Trivizas, M. A. Karakassides, M. Baikousi, A. Kouloumpis, D. Gournis, A. Bakandritsos, K. Hola, O. Kozak and R. Zboril, *Carbon*, 2015, **83**, 173–179.
126 Z. Qian, J. Ma, X. Shan, H. Feng, L. Shao and J. Chen, *Chem. Eur J.*, 2014, **20**, 2254–2263.
127 F. Wang, Z. Gu, W. Lei, W. Wang, X. Xia and Q. Hao, *Sens. Actuators, B*, 2014, **190**, 516–522.
128 L. Zhao, H. Li, Y. Xu, H. Liu, T. Zhou, N. Huang, Y. Li and L. Ding, *Anal. Bioanal. Chem.*, 2018, **410**, 4301–4309.